

MD-PhD Thesis

Molecular physiology of the inner hair cell ribbon synapses

Submitted by

Khimich Darina

Göttingen, 2005

Declaration

**The thesis has been written independently and with no other sources and aids than
quoted.**

**Darina Khimich
14th March 2005**

Contents

Abbreviations	4
1. Introduction	6
1.1 The mammalian ear	6
1.2 Anatomy and functional aspects of the cochlea	8
1.3 The organ of Corti	12
1.4 The inner hair cells	15
1.5 The synaptic ribbon	19
1.6 Aim of this work	21
2. Materials and methods	23
2.1 Animals	23
2.2 Genotyping	23
2.3 Preparation of the organ of Corti	24
2.4 Solutions	25
2.5 Cell electrophysiology	26
2.5.1 The patch-clamp setup	26
2.5.2 The patch-clamp of inner hair cells	27
2.5.3 Capacitance measurements	30
2.5.4 Data analysis	30
2.6 Immunocytochemistry	31
2.6.1 Antibodies	31
2.6.2 Buffers	32

Contents

2.6.3	Immunostaining procedure	32
2.6.4	Confocal microscopy	33
2.6.5	Data analysis	33
3.	Results	35
3.1	Localization of Bassoon in the mouse organ of Corti	35
3.2	Loss of Bassoon function in adult inner hair cells causes hearing impairment - synaptic audiopathy	37
3.2.1	Gross cochlear morphology of Bassoon mutants	37
3.2.2	Ultrastructural changes in the IHCs of Bassoon mutants	38
3.2.2.1	IHCs at electron microscopy level	38
3.2.2.2	Analysis of “ribbon-containing” synapses with confocal microscopy	43
3.2.2.3	Investigation of ribbon morphology	45
3.2.3	IHC electrophysiology	46
3.2.3.1	Ca ²⁺ -current, exocytosis and endocytosis	46
3.2.3.2	K ⁺ -currents	51
3.2.4	Auditory morphophysiological correlation in Bassoon mutants	52
3.3	Bassoon inner ear phenotype during development	55
3.3.1	Bassoon phenotype at the onset of hearing	55
3.3.1.1	Synaptic organisation of the IHCs in young hearing mice	55
3.3.1.2	Cell electrophysiology in 3-week-old mice	55
3.3.1.2.1	Ca ²⁺ -current and exocytosis of the IHCs	55
3.3.1.2.2	Endocytosis in young IHCs	58

Contents

3.3.2	Analysis of Bassoon mutants before the onset of hearing	58
3.3.3	3.3.2.1 Patch clamp measurements of the immature IHCs	58
3.4	Structure-function relationship of afferent wild type and mutant cochlear synapses during development	61
4.	Discussion	63
4.1	Molecular anatomy of the hair cell ribbon synapse	63
4.2	Phenotype of Ca ²⁺ and K ⁺ currents in Bassoon mutants	65
4.3	Mechanism of exocytosis at the IHC ribbon synapses – lessons from the Bassoon mutant	66
4.4	Bassoon mutants – a mouse model for synaptic audiopathy	69
5.	Conclusion	71
6.	References	72
	Acknowledgements	82
	Curriculum vitae	83

Abbreviations

Abbreviations:

ABR - auditory brainstem responses

ATP - adenosine 5'-triphosphate

AMPA - α -amino-3-hydroxy-5-methyl-4-isoxazolepropionic acid

BARS - Brefeldin A adenosine diphosphate ribosylated substrate

BK channels - large -conductance Ca^{2+} -activated K^{+} -channels

CAZ - cytomatrix at the active zone

C_m - membrane capacitance

C_p - pipette capacitance

CtBP - C-terminal binding protein

DNA - deoxyribonucleic acid

DPOAE - distortion product otoacoustic emissions

EGTA - ethylene glycol-bis-(2-aminoethyl)-N,N,N', N'-tetraacetic acid

GABA - gamma-aminobutyric acid

GluR - glutamate receptor

GSDB - goat serum dilution buffer

GTP - guanosine 5'-triphosphate

IHC - inner hair cell

OHC - outer hair cell

PBS - phosphate buffer solution

PCR - polymerase chain reaction

RRP - readily releasable pool

R_m - membrane resistance

Abbreviations

R_s - series resistance

SGN - spiral ganglion neuron

TEA - tetraethylammonium chloride

WT – wild-type

1.Introduction

1.1 The mammalian ear

Sound consists of the mechanical vibrations transmitted by an elastic medium. Sound carries energy through the air at a speed of about 340 m/s. To hear, our ears must capture this mechanical energy, transmit it to the ear's receptive organ, the Cochlea, and transduce it into electrical signals suitable for analysis by the nervous system (reviewed in Dallos et al., 1996; Kandel et al., 2000). These three tasks are the functions in mammals of the external ear, the middle ear, and the inner ear (Fig. 1.1).

The external (outer) ear consists of the auricle and the external auditory meatus (the ear canal). The auricle is a prominent fold of cartilage-supported skin and acts as reflector to capture sound efficiently and to focus it into the external auditory meatus. Our capacity to localize sounds in space depends critically upon the sound-gathering properties of the external ear. The ear canal ends at the tympanum (tympanic membrane, eardrum), a thin diaphragm that separates the outer ear and the middle ear and vibrates to sound.

The middle ear is an air-filled cavity connected to the pharynx by the Eustachian tube. It contains three tiny interconnected bones: the malleus (hammer), the incus (anvil), and the stapes (stirrup). The base of the malleus is attached to the tympanic membrane and its other extreme makes a ligamentous connection to the incus, which is similarly connected to the stapes. The flattened termination of the stapes, the footplate, inserts in a hole (the oval window) of the bony covering of the cochlea. Sound-induced vibrations of the tympanic membrane are transmitted to the oval window of the fluid-filled cochlea by the middle ear ossicles. The other functions of the middle ear are: first, to amplify the sound that reaches the

Introduction

cochlea, which it does by impedance matching; sound pressure is preserved through the middle ear because the surface area of the tympanic membrane is about 35x the surface of the

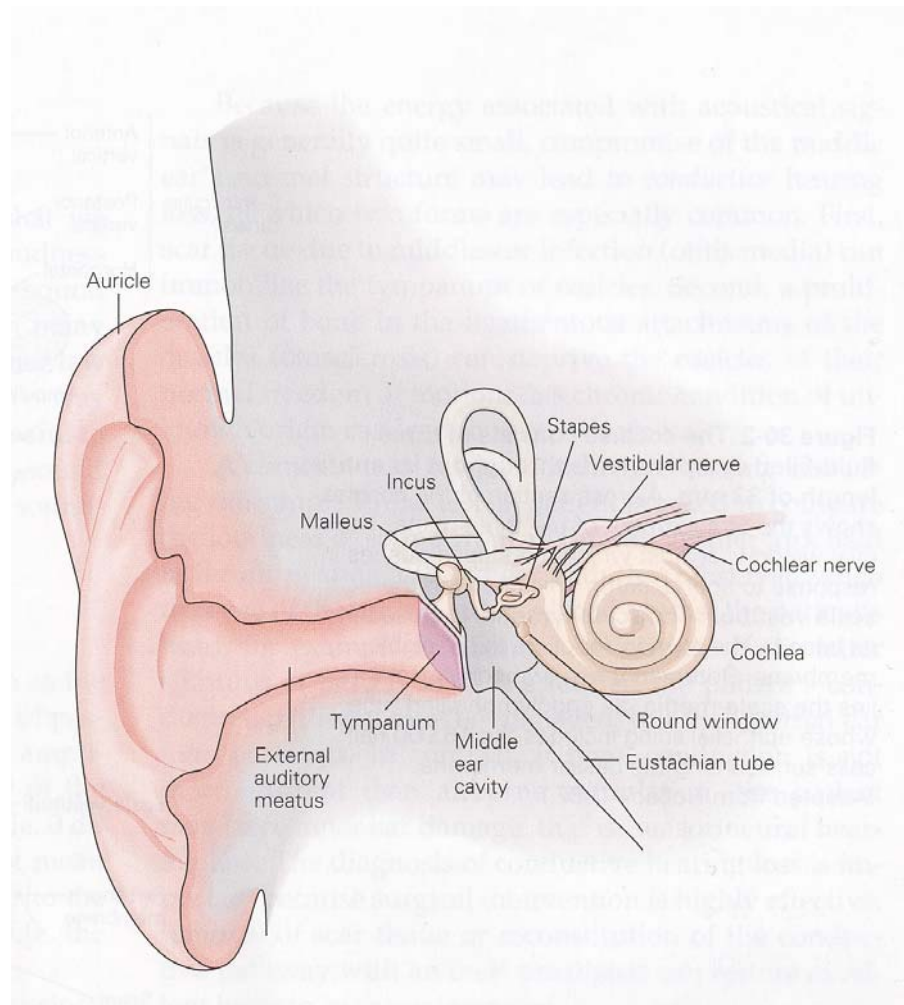


Figure 1.1. The structure of the human ear. The external ear, especially the prominent auricle, focuses sound into the external auditory meatus. Alternating increases and decreases in air pressure vibrate the tympanum. These vibrations are conveyed across the air-filled middle ear by three tiny, linked bones: the malleus, the incus, and the stapes. Vibration of the stapes stimulates the cochlea, the hearing organ of the inner ear (from Kandel et al., 2000).

Introduction

oval window, so 35x as much force is exerted by sound at the membrane. Second, it adjusts the amplitude of ossicle vibrations to the average sound level by using muscles: tensor tympani muscle (when it contracts, it increases the tension of the tympanic membrane that decreases the transmission of vibration), and the stapedial muscle (it contracts in response to a loud noise and decreases the transmission of vibration), which protect the delicate inner ear from sound damage. Its third function is to equalize the average pressure across the tympanic membrane equal to the air pressure in the environment via the Eustachian tube (Fig. 1.1).

The inner ear (labyrinth) is a complex structure consisting of two major parts: the cochlea, the organ of hearing; and the vestibular system, the organ of balance. The vestibular system consists of the saccule and the utricle, which determine stationary position sense, and the semicircular canals, angular acceleration detectors in three perpendicular planes, which help to maintain balance.

1.2 Anatomy and functional aspects of the cochlea

The cochlea derives its name from the *Cochlea*, the Latin word for snail. A human cochlea consists of about 2.5 coils of progressively diminishing diameter turned around a bony core, the modiolus and is stacked in a conical structure like a snail's shell, Fig. 1.2 (Kandel et al., 2000). The number of coils depends on the species. Thus, the mouse has 1.75 coils, the guinea pig 4, and the bird 0.75 turns. Covered with a thin layer of laminar bone, the entire cochlea is localized within the dense structure of the temporal bone. The interior of the cochlea consists of the three fluid-filled tube-like compartments: scala vestibuli, scala tympani and scala media.

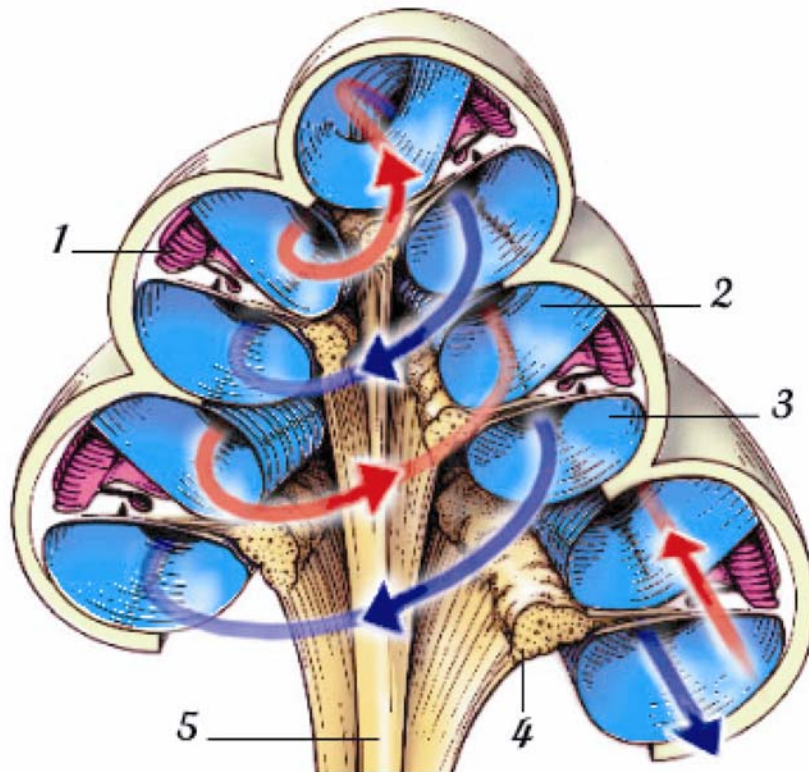


Figure 1.2. Schematic sagittal section of the cochlea. On the axial section of the cochlea through the modiolus could be observed the arrangement of three fluid filled compartments: 1- scala media, filled with endolymph, 2- scala vestibuli, filled with perilymph, 3- scala tympani, filled with perilymph. The colour arrows point towards the direction of fluid displacement upon stimulation and interconnection between scala vestibuli and scala tympani via helicotrema at the apical part of cochlea. 4- cell bodies of the spiral ganglion neurons; 5- cochlear nerve (from Pujol et al., <http://www.iurc.montp.inserm.fr/cric/audition>).

Scala vestibuli, the perilymph-filled spirally arranged canal in the bony tube of the cochlea is separated from the scala media below by Reissner's membrane and receives vibrations from the stapes through the oval window (Fig. 1.1). The lowermost of the three chambers, the scala tympani that is separated from the scala media by the basilar membrane, has also a

Introduction

basal aperture, the round window, which is closed by an elastic diaphragm. The scala vestibuli and scala tympani are filled with the perilymph (extracellular-like fluid; Table 1) and communicate with one another at the helicotrema, an interruption of the cochlea duct at

Component	Cochlea endolymph	Perilymph of the scala vestibula	Perilymph of the scala tympani	Plasma
Na ⁺ (mM)	1.3	141	148	145
K ⁺ (mM)	157	6.0	4.2	5.0
Ca ²⁺ (mM)	0.023	0.6	1.3	2.6
Cl ⁻ (mM)	132	121	119	106
HCO ₃ ⁻ (mM)	31	18	21	18
Glucose (mM)	0.6	3.8	3.6	8.3
Protein (mg/100 ml)	38	242	178	4238

Table 1. Averages of the inner ear fluid composition obtained in guinea pig and rodents. Only the most abundant components are listed in this table. According to convention, values in the table are “activities” for Ca²⁺, but concentrations for other constituents. The activity of an ion indicates its unbound, dissociated ionic form, i.e., the form that is generally available for biological reactions and thus determines its physiological activity (modified from Dallos et al., 1996)

the cochlea apex. The kinetics of tracers entering perilymph from blood (Ferrary et al. 1987) and the quantitative differences between the composition of perilymph and plasma (Thalmann et al., 1992) suggests that the perilymph mainly originates from a transcellular

Introduction

transport of solutes from blood rather than by serum ultrafiltration. The scala media is filled with the endolymph, which has a composition similar to that of the intracellular fluid (Table 1). The ionic composition of endolymph is a product of active transport processes in the stria vascularis, a highly vascularized multilayered epithelium adjacent to the spiral ligament in the lateral wall of the cochlea (for review see Marcus et al., 2002). This active transport of K^+ generates the endocochlear potential of about +80 mV between scala media and scala vestibula/tympani that provides the energy for mechanoelectrical transduction in the hair cells (Dallos et al., 1973).

The basilar membrane, the elastic structure separating scala media and scala tympani is not uniform. Instead, it is thinner, broader and more floppy at the apex of the cochlea but thicker, more narrow and stiff toward the base.

The action of the stapes upon sound at the oval window produces pressure changes that propagate throughout the fluid of the scala vestibuli at the speed of sound. Because the aqueous perilymph is virtually incompressible, the primary effect of the stapes's motion is to displace the fluid in the scala vestibuli toward the elastic cochlea partition (toward the scala media). This motion in turn increases the pressure in the scala tympani and displaces a fluid mass that causes outward bowing of the round window. Each cycle of a sound stimulus thus evokes a complete cycle of up-and-down movement of fluid in each of three chambers of the inner ear. Due to anatomical properties of the basilar membrane this motion does not cause equal movement of the entire basilar membrane but rather reaches maximal amplitude at the position appropriate for the frequency of stimulation and then rapidly declines in size. Thus at the apex of the human cochlea the basilar membrane responds best to the lowest

frequencies that we can hear (down to approximately 20 Hz) and at the cochlea base resonates to vibrations as great as 20 kHz (e.g. tonotopic organization of the cochlea).

1.3 The organ of Corti

The organ of Corti, the hearing receptor organ, is localized on the basilar membrane and faces the highly differentiated sensory epithelium (hair cells) towards the scala media (Fig. 1.3). It consists of one row of inner hair cells, three rows of outer hair cells and several types of supporting cells (e.g. pillar cells, Deiters' cells, Hensen cells, etc.).

While supporting cells play a homeostatic and mechanical support role, the OHCs provide active amplification of the sound energy (reviewed in Hudspeth et al., 1997, Dallos and Fakler, 2002). The OHCs have distinctive hair bundles (stereocilia), which are the mechanosensory input organelle of these cells. When mechanically stimulated by incoming sound waves, the ciliary bundle is deflected, and thereby open mechanosensitive ion channels in the stereocilia membrane that cause influx of cations (mainly K^+) and depolarization of the OHC (Hudspeth and Corey, 1977). But, unlike all other hair cells, OHCs then translate the resulting changes in membrane potential into macroscopic changes of the length of their cylindrical cell bodies (Kachar et al., 1986; Evans and Dallos, 1993). Depolarization triggers cell contraction, whereas hyperpolarization results in cell elongation (Kachar et al., 1986). This electrically driven cell motility, called electromotility, presumably occurs in a cycle-by-cycle mode (that is, responding on each cycle of the sound stimulus, Frank et al., 1999) over the entire range of acoustic frequencies, if feeds energy back into the vibrating basilar membrane and thereby amplifies its motion (Ashmore, 1987). The underlying mechanism of electromotility was recently elucidated by the team of Peter Dallos, when the function of the

Introduction

membrane protein prestin as a transmembrane motor protein was first described (Zheng et al., 2000). Prestin belongs to an anion transporter family SLC26 (Zheng et al., 2002; Lohi et al., 2000). In response to transmembrane voltage changes, prestin undergoes conformational changes that lead to the length changes of the OHCs (Oliver et al., 2001). Thus, electromotility driven by prestin could underlie cochlear amplification (Liberman et al., 2002). However, generation of force by hair bundle itself might represent another mechanism for active amplification of sound-induced cochlear vibration (Chan and Hudspeth, 2005; Kennedy et al., 2005).

The organ of Corti is innervated by the auditory nerve, which is part of the VIIIth cranial nerve. The afferent information is transmitted via neurotransmitter release by synaptic vesicle exocytosis at the active zones of IHCs (and maybe the OHCs) onto the auditory nerve fiber boutons (the spiral ganglion fibers). The cell bodies of the spiral ganglion neurons (SGN) are localized within the modiolus and send their processes to the Cochlear nucleus in the medullo-pontine junction of the brainstem. There are two types of SGN fibers (reviewed in Eybalin, 1993; Raphael and Altschuler, 2003; Dallos et al., 1996). The thick myelinated type I SGN fibers receive auditory information from IHCs and comprise 90-95% of the SGN population. The type I SGN has only one peripheral process, which contacts a single IHC, while each IHC receives connections from multiple (10-30) SGNs (Liberman, 1982; Liberman et al., 1990). The thin unmyelinated type II SGN fibers have synaptic connection with the OHCs (Brown, 1987). As far as some vesicles and ribbon synapses have been seen in the OHCs only at the apical turn or during development, the main function of the SGNs is probably to contribute to an efferent feed-back loop (Raphael and Altschuler, 2003). The efferent innervation of the IHCs and OHCs is provided by lateral olivocochlear (the inner

Introduction

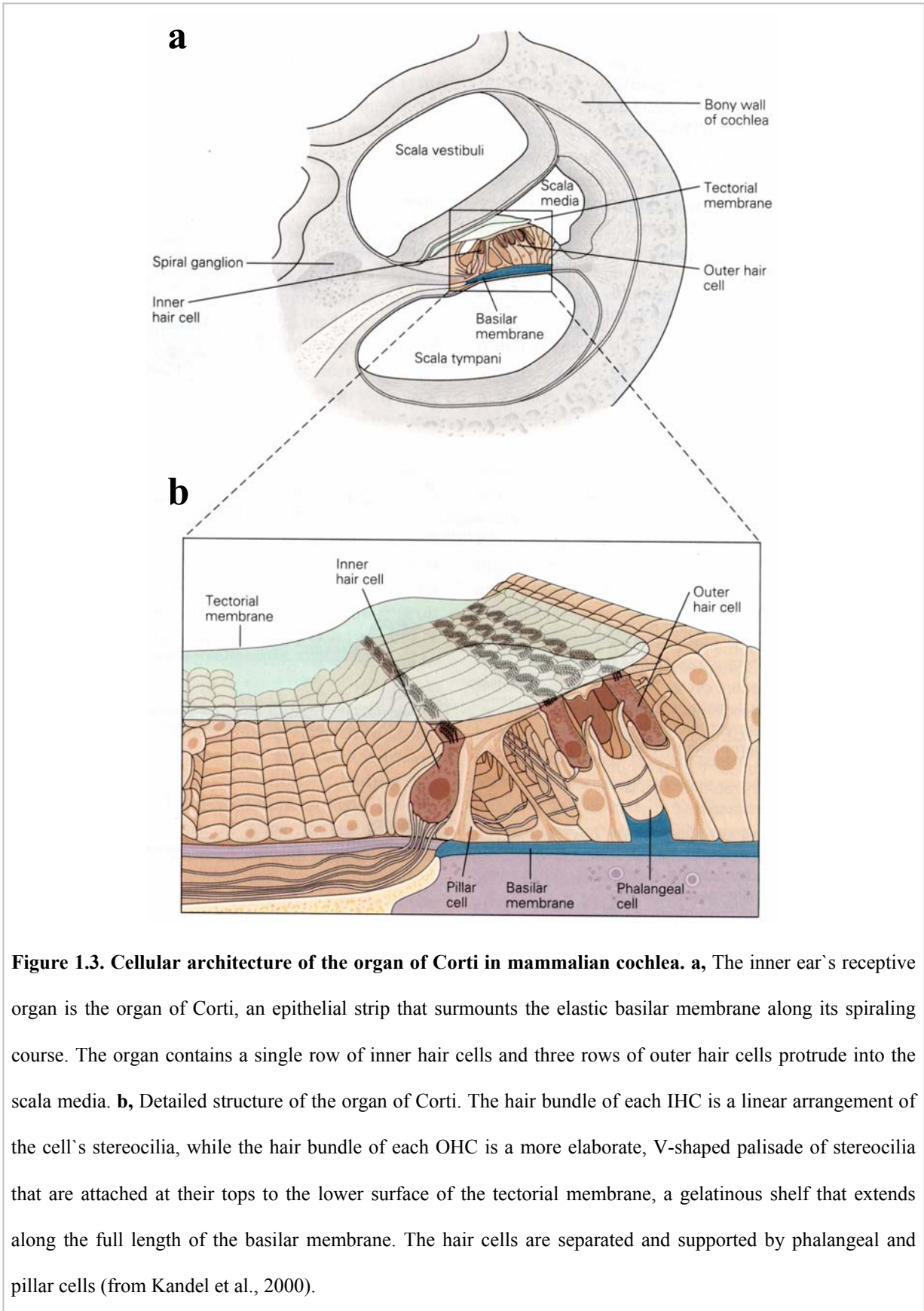


Figure 1.3. Cellular architecture of the organ of Corti in mammalian cochlea. a, The inner ear's receptive organ is the organ of Corti, an epithelial strip that surmounts the elastic basilar membrane along its spiraling course. The organ contains a single row of inner hair cells and three rows of outer hair cells protrude into the scala media. **b,** Detailed structure of the organ of Corti. The hair bundle of each IHC is a linear arrangement of the cell's stereocilia, while the hair bundle of each OHC is a more elaborate, V-shaped palisade of stereocilia that are attached at their tops to the lower surface of the tectorial membrane, a gelatinous shelf that extends along the full length of the basilar membrane. The hair cells are separated and supported by phalangeal and pillar cells (from Kandel et al., 2000).

spiral bundle) and medial olivocochlear (the outer spiral bundle) fibers respectively. The lateral olivocochlear efferents arise in the lateral superior olive (White and Warr, 1983; Guinan et al., 1984) and contact with IHCs during development, but upon the onset of hearing (between two and three weeks postnatal) they terminate only on dendritic endings of type I SGN beneath the IHCs (Emmerling et al., 1990; Sobkowicz and Slapnick, 1994; Simmons et al., 1996). The mechanism of efferent axodendritic transmission has not been entirely elucidated. Evidences exist for several transmitters to be involved, including acetylcholine, dynorphin, calcitonin-gene related peptide, enkephalin, dopamine and GABA (reviewed in Eybalin, 1993). The lateral olivocochlear fibers probably modulate the type I SGN activity and spontaneous activity of the IHCs during development (Glowatzki and Fuchs, 2000). The medial olivocochlear efferents arise from the ventral nucleus of the trapezoid body and medially located superior olivary complex nuclei and terminate at the bases of OHCs (Guinan et al., 1984). They release mainly acetylcholine causing a hyperpolarization of the OHCs, thus modulating hair cell motility and changing the gain of the cochlear amplifier (Eybalin, 1993).

1.4 The inner hair cell

The IHCs could be recognized as one row of highly specialized pear shaped neuroepithelial cells with a hair bundle on their apical parts (Fig. 1.3b, 1.4). Each IHC has 20-50 (or more) hair bundles (stereocilia), depending on the species and the location along the cochlear duct, with more stereocilia closer to its basal end that are arranged in two or three rows (reviewed in Raphael and Altschuler, 2003). Stereocilia of hair cells are cylindrical protrusions with an actin-based scaffold (Sobin and Flock, 1983). The apical tip

Introduction

of the hair bundle is connected to its neighbouring stereocilia with a tip link filament (Pickles et al., 1984) that contacts mechanical channels in the stereocilia membrane and is partially made of Cadherin 23 (Sollner et al., 2004; Siemens et al., 2004). The mechano-electrical transduction ion channels of hair cells are relatively nonselective, cation-passing pores with a conductance near 100 pS and belong to the transient receptor potential channels superfamily (Corey et al., 2004). Movement of the hair cell stereocilia upon sound vibrations in the cochlea opens transduction channels, allowing ion entry (mainly K^+ as the most abundant in endolymph) and generating transduction current (reviewed in Hudspeth, 1997).

Beside the mechanotransduction channels, the IHCs also contain Ca^{2+} -channels, K^+ -channels and during development transiently express Na^+ -channels (reviewed in Dallos et al., 1996). About 92% of all IHCs Ca^{2+} -channels are represented by $Ca_v1.3$ ($\alpha 1D$) L-type channels and the remaining probably belong to the $Ca_v1.4$ channel type (Platzer et al., 2000; Brandt et al., 2003). Ca^{2+} -current upon depolarization is low at birth, reaches its maximum at p6 and at p12 decreases to adult values (Beutner and Moser, 2001; Brandt et al., 2003; Johnson et al., 2004). Under physiological conditions Ca^{2+} -channels are opened by a graded receptor potential upon influx of cations through mechanotransduction channels during sound-induced vibrations in the cochlea. However, before the onset of hearing the IHCs could fire Ca^{2+} action potentials (Kros et al., 1998; Glowatzki and Fuchs, 2000; Beutner and Moser, 2001). It is suggested that Ca^{2+} -channels are predominantly distributed at the basolateral parts of the hair cell and colocalized to release sites (Roberts et al., 1990; Martinez-Dunst et al., 1997; Brandt et al., unpublished data). Ca^{2+} influx through L-type Ca^{2+} -channels triggers the fusion of presynaptic vesicles and release of the neurotransmitter onto the postsynaptic terminals (Fuchs et al., 1990; Roberts et al., 1990; Moser and Beutner,

Introduction

2000). The mouse mutants deficient of $Ca_v1.3$ are deaf and finally undergo degeneration of afferent auditory nerve fibers and hair cells (Platzner et al., 2000; Brandt et al., 2003).

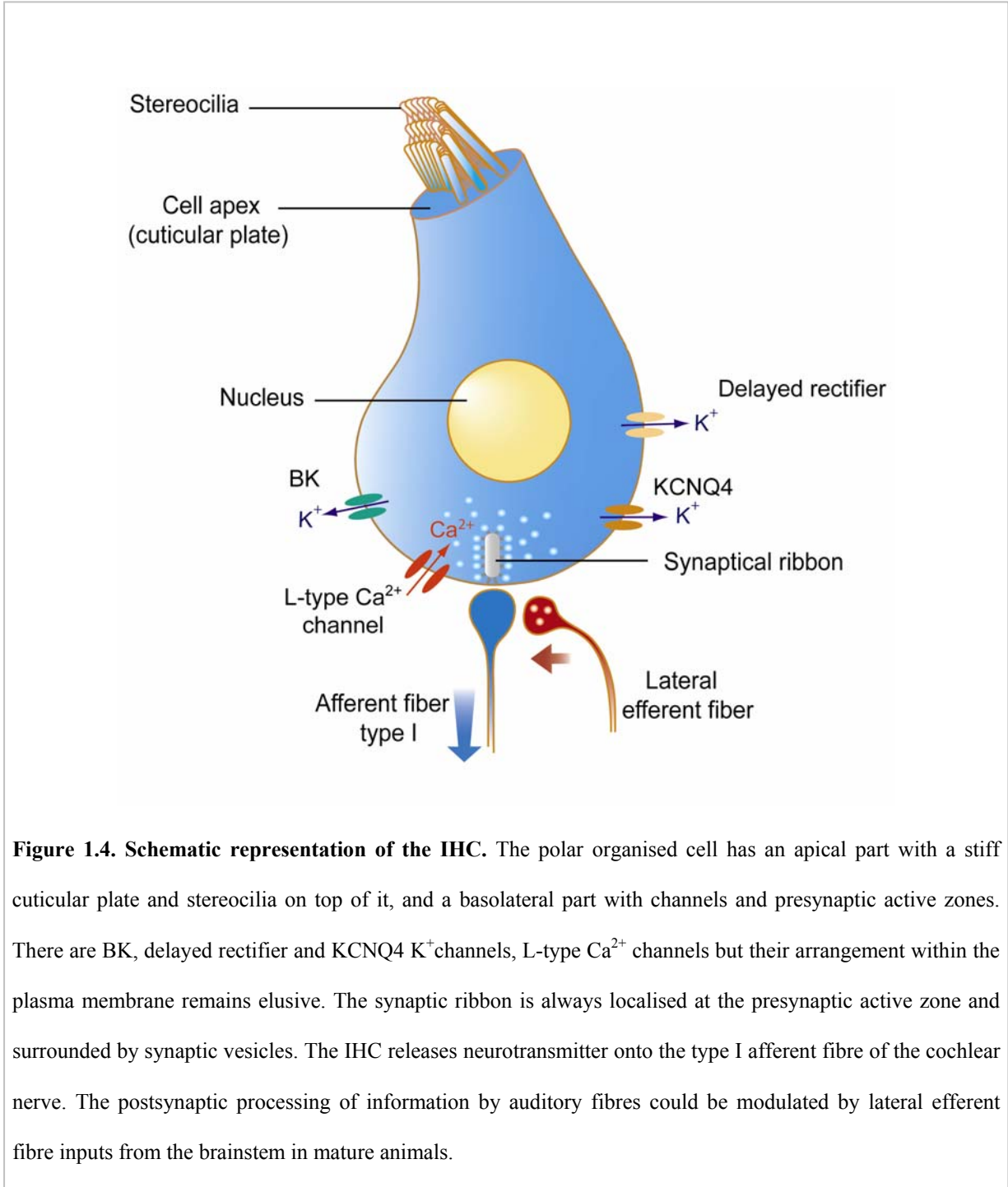


Figure 1.4. Schematic representation of the IHC. The polar organised cell has an apical part with a stiff cuticular plate and stereocilia on top of it, and a basolateral part with channels and presynaptic active zones. There are BK, delayed rectifier and KCNQ4 K^+ channels, L-type Ca^{2+} channels but their arrangement within the plasma membrane remains elusive. The synaptic ribbon is always localised at the presynaptic active zone and surrounded by synaptic vesicles. The IHC releases neurotransmitter onto the type I afferent fibre of the cochlear nerve. The postsynaptic processing of information by auditory fibres could be modulated by lateral efferent fibre inputs from the brainstem in mature animals.

Introduction

K⁺-channels of adult mammalian IHCs include large -conductance Ca²⁺-activated (BK), delayed rectifier (K_v), and KCNQ4 (Fig. 1.4). The TEA-sensitive BK current has submillisecond activation, huge amplitude and first appears in IHCs around p12 postnatal, just at the onset of hearing in mice (Kros and Crawford, 1990; Marcotti et al., 2003; Langer et al., 2003). The slow outward 4-aminopyridine-sensitive current is thought to be carried by delayed rectifier (K_v, or I_{Ks}) K⁺ channels (Kros and Crawford, 1990; Marcotti et al., 2003). The functional role of both currents is to shape the receptor potential of the IHCs (Kros et al., 1998). The KCNQ4 K⁺-channel, whose expression has been recently described in the IHCs shows low voltage activation and sets the resting potential and submembrane Ca²⁺ concentration of the cell (Marcotti et al., 2003; Oliver et al., 2003; Kharkovets et al., unpublished data). Mutations in the KCNQ4 K⁺ channel gene have been shown to underlie a form of autosomal dominant progressive hearing loss classified as DFNA2 (Kubisch et al., 1999).

The soma of the IHC (Fig. 1.4) has a centrally located nucleus, a well developed endoplasmic reticulum and Golgi complex and is tightly filled with small synaptic vesicles (reviewed in Dallos et al., 1996). While the apical part of the cell is specialized for mechano-electrical transduction, the basolateral is organized for transmission of the signal onto the auditory nerve. The neurotransmitter of the IHCs is most likely to be glutamate (Kataoka and Ohmori, 1996; Matsubara et al., 1996; Glowatzki and Fuchs, 2002). Exocytosis of docked vesicles is stimulated by Ca²⁺ (Moser and Beutner, 2000; Beutner et al., 2001), but is adapted for a high rate synaptic transmission for a long period of time, which is probably due to a special synaptic organization of the IHCs - the ribbon synapses.

1.5 The synaptic ribbon

The synaptic ribbon is a submicron, electron-dense organelle in the terminals of vertebrate photoreceptors and bipolar cells of retina, in auditory and vestibular hair cells, and in pinealocytes (reviewed in Lenzi and Gersdorff, 2001; Fuchs et al., 2003; Lagnado et al., 2003, Sterling and Matthews, 2005). In fish and amphibians, they also occur in the hair cells and electroreceptors of the lateral line (Wagner, 1997). In addition, similar structures are common in the neuromuscular junction of some invertebrates (Katz et al., 1993). In fact, the ribbon seems to occur wherever synaptic exocytosis is evoked by graded depolarization and where signaling requires a high rate of sustained release. Synaptic ribbons are named for their appearance as electron-dense bars in cross-section in electron micrographs (Fig. 1.4). However, ribbons can assume different shapes in the same cell types between species (Lysakowski, 1996), within a cell type across one tissue (Siegel and Brownell, 1981; McNulty and Fox, 1992; Merchan-Perez and Liberman, 1996) or even within the same region depending on activity conditions (Spiwoks-Becker et al., 2004).

All synaptic ribbons are osmiophilic, lack a delimiting membrane, and are surrounded by a halo of clear-core vesicles. Electron-lucent vesicles of about 35 nm diameter are either attached directly to the ribbon with 1-5 thin 20 nm long filaments or concentrated in the immediate surrounding cytoplasm by as yet unknown means (Lenzi et al., 1999; Lenzi et al., 2002, Usukura et al., 1987). From the morphological characteristics of ribbons (their proximity to the active zone and close association with vesicles) it has long been supposed that these organelles play an important role in exo- and endocytosis (reviewed Wagner, 1997; von Gersdorff and Matthews, 1999). On the basis of capacitance measurements of vesicular release it has been proposed that either vesicles at the base of the ribbon and attached to the

Introduction

plasma membrane (Moser and Beutner, 2000; von Gersdorff, 2001) or all vesicles connected to ribbons (Edmonds et al., 2004; Spassova et al., 2005) comprise the readily releasable pool (RRP) of vesicles. Vesicles in this pool appear to have undergone all of the priming reactions that are essential for exocytosis, because the whole pool can be released in the absence of ATP hydrolysis (Beutner et al., 2001; Heidelberger et al., 2002). It has been speculated that ribbons might serve as a “conveyor belt” (Vollrath and Spiwox-Becker, 1996) that actively moves vesicles toward their release sites, but the exact role of these organelles in transmitter release remains unclear.

The molecular components of the ribbon have only recently begun to be identified mainly in the retina. First, there is RIBEYE, which is composed of an N-terminal A domain and a C-terminal B domain (Schmitz et al., 2000). The B domain is transcribed from the same gene as the transcriptional repressor C-terminal binding protein 2 (CtBP2) that only differs from the RIBEYE B-domain by 20 N-terminal amino acids (Schmitz et al., 2000). Second, there is RIM, which is present at all synapses and interacts with rab3, a GTPase expressed on synaptic vesicles (Wang et al., 1997; Hibino et al., 2002). Third, there is immunostaining evidence for the presence of KIF3A, a kinesin motor in retinal ribbons (Muresan et al., 1999). Finally, there are Bassoon and Piccolo, giant presynaptic cytomatrix proteins, 420 and 550 kDa large, respectively (tom Dieck et al., 1998; Wang et al., 1999; Fenster et al., 2000), which are implicated in the structural and functional organization of the active zone in both excitatory and inhibitory synapses and have evolved only in vertebrates (Wang et al., 1999; Fenster et al., 2000). During development they are among the earliest presynaptic proteins to appear at newly formed synapses (Zhai et al., 2001). Bassoon and Piccolo are both expressed at photoreceptor ribbons, but only Piccolo is expressed at bipolar ribbons (Dick et al., 2001).

Interestingly, Bassoon was found to be colocalized to the base of photoreceptor ribbon, whereas Piccolo immunogold staining was concentrated at the apical region of the ribbon (Dick et al., 2001). Generation of mice lacking almost the entire core region of Bassoon (deletion removed amino acids from 505 to 2889) revealed new opportunities for studying the function of this protein. The mutant mice suffer from epileptic seizures, from which they die usually during 6 months, have a reduced number of fusion-competent vesicles and an increased number of silent synapses in the hippocampus (Altrock et al., 2003). Moreover, Piccolo levels in the brain are upregulated (Altrock et al., 2003). The photoreceptor ribbons of the mutants are not anchored to the presynaptic active zones, which results in impaired vision (Dick et al., 2003). However, the specific role of the ribbon in transmitter release remained elusive, because synaptic pathophysiology could not be explored at the level of the photoreceptors (Dick et al., 2003).

1.6 Aim of this work

Although ribbon synapses are the key element for transmission of sensory information, so far we have limited knowledge about their organization and function. In close collaboration during this study we:

1. Showed expression of Bassoon, RIBEYE and Piccolo in the ribbons of IHCs;
2. Characterized the auditory phenotype of Bassoon mouse mutants;
3. Used Bassoon mutation, natural developmental changes in the IHCs and combination of different techniques (immunocytochemistry with confocal and 4Pi imaging, electron microscopy, patch-clamp technique with capacitance measurements, *in vivo*

Introduction

investigation of the auditory system) to elucidate the fundamental role of ribbons in synchronous auditory signalling;

4. Described a mouse model for synaptic audiopathy.

2. Materials and methods

2.1 Animals

The Bassoon mutant mice were generated by tom Dieck et al. (Altrock et al., 2003; Dick et al., 2003) at the Leibniz Institute for Neurobiology, Magdeburg, Germany. A *lacZ/neo* cassette with an internal ribosome entry site for the *lacZ* transcript and a PGK promoter for the *neo* cassette was cloned into exon 4 and intron 5 of Bsn genomic DNA to replace half of exon 4 and the entire 6.6 kb of exon 5. Gene targeting and generation of the mouse line was performed as described (Talts et al., 1999).

For our study we tested Bassoon mutant mice as well as their wild type and heterozygous littermates at the age from 1 to 8-week-old.

All animal experiments were performed in compliance with the guidelines for the welfare of experimental animals issued by the Federal Government of Germany, the NIH, and the Max Planck Society.

2.2 Genotyping

The genotyping was performed on all animals prior to the investigations and repeated after the experiments. The DNA was extracted from the small tail biopsies (~5 mg) using a standard protocol (<http://www.gentra.com/pdf/00708.pdf>) and the Puregene DNA purification mouse tail kit (Gentra).

Mice were genotyped by PCR reactions in 12.5 μ l final volumes. The standard PCR mixture contained: the PCR buffer (20 mM Tris/HCl, pH 8.4, 50 mM KCl; Invitrogen), 3 mM MgCl₂, 1 pmol/ μ l of the sense and the antisense primers, 200 μ M dATP, 200 μ M dCTP,

Materials and methods

200 μ M dGTP, 200 μ M dTTP (Amersham Pharmacia Biotech), 250 ng of the template DNA and 0.625 units of the Taq-DNA-polymerase recombinant (Invitrogen). The wild type forward and reverse primers were (KOS1-) GGTATCCTGTTCTGAAAGACTT and (pWHAS1-) AAGCTTGATATCGAATTTGGCCT; the mutant primers were (V2-) AGTTGTCAAGCCTGTTCCAGAAGC and (V3-) ACACCGTCGGAGGAGTAGCCTGT. Amplification for the wild type primers was started with incubation for 5 minutes at 94°C followed by 30 amplification cycles (30 sec at 94°C, 45 sec at 67°C, 60 sec at 72°C) then 2 minutes at 72°C and cooled down to 4°C. The protocol for the mutant primers was: 5 minutes at 94°C followed by 30 amplification cycles (30 sec at 94°C, 45 sec at 64°C, 60 sec at 72°C), 2 minutes at 72°C and cooled down to 4°C.

The DNA fragments were separated by agarose gel electrophoresis. 2% agarose gels were prepared with TBE buffer (Carl Roth). The DNA gels were stained with SYBR (green I nucleic acid gel staining, Cambrex, Cat.Nr. 50513) diluted 1:10000 in TBE, and the DNA bands were visualized under ultraviolet light. Genotyping of the wild-type animals revealed the PCR bands of 600 bp, while the mutant mice were characterized by the PCR bands at 400 bp and heterozygous mice showed both bands.

2.3 Preparation of the organ of Corti

The mice were killed by decapitation, the skull sagittally cut into two parts that were placed into Petri dishes with ice-cooled Hank's solution. Under the dissecting microscope, the brain was removed and the bulla was opened to expose the cochlea. The cochlea's bony envelope was carefully opened and the apical coil of the organ of Corti was removed with fine forceps. The stria vascularis of adult mice (more than 3 weeks old) usually attached to the bony

Materials and methods

capsule of the cochlea was separated from the organ of Corti when removing the bones. However, the p6 organ of Corti preparations frequently remained attached to the stria vascularis and had to be carefully peeled off.

The apical coil of the organ of Corti was transferred by a Pasteur pipette into the recording chamber containing ice-cooled Ringer solution. The organ of Corti was fixed on the bottom of the chamber by a grid of nylon threads, with the stereocilia pointing upwards and the basilar membrane downwards.

To approach the cells, the tectorial membrane was removed with a big cleaning pipette at the patch-clamp setup. To access the IHCs from the modiolar side, the neighboring cells were gently removed with patch pipettes ($R_s \sim 3\text{-}5\text{ M}\Omega$).

2.4 Solutions

The **HEPES-HANKS** solution for preparation of the organ of corti contained (in mM): 141 NaCl, 5.4 KCl, 1 MgCl₂, 0.5 MgSO₄, 6 L-Glutamine, 7 Glucose, and 10 NaOH-HEPES.

The extracellular **modified Ringer** saline used for measurements of Ca²⁺ current, exocytosis and endocytosis contained (in mM): 105 NaCl, 2.8 KCl, 1 MgCl₂, 10 NaOH-HEPES, 10 CaCl₂, 35 TEA-Cl, and 10 D-glucose. For the experiments on 8-week-old wild type animals with low Ca²⁺-concentration (2 mM CaCl₂) 8 mM CaCl₂ were replaced by NaCl.

The extracellular **Ringer** saline used to measure K⁺-currents contained (in mM): 140 NaCl, 2.8 KCl, 1 MgCl₂, 10 NaOH-HEPES, 2 CaCl₂, and 10 D-glucose.

The **intracellular solution for perforated patch** experiments contained (in mM): 140 Cs-gluconate, 13 TEA-Cl, 10 CsOH-HEPES, 1 MgCl₂. Amphotericin B in the amount of 250

$\mu\text{g/ml}$ was added freshly to the intracellular solution before the experiment and mixed by sonication.

The **intracellular solution for whole-cell** recordings of K^+ -current contained (in mM): 150 KCl, 10 KOH-HEPES, 1 MgCl_2 , 2 Mg-ATP and 0.3 Na-GTP.

The **intracellular solution for whole-cell** with EGTA contained (in mM): 140 Cs-gluconate, 13 TEA-Cl, 10 CsOH-HEPES, 1 MgCl_2 , 2 Mg-ATP and 0.3 Na-GTP and 5 EGTA.

The pH for all solutions was adjusted to 7.2. All salines had osmolarities between 300 and 320 mmol/l.

The chemicals for solutions were obtained from Sigma-Aldrich except for Amphotericin B (Calbiochem). Cs-gluconate salt was prepared in our laboratory from CsOH and D-gluconic acid solutions.

2.5 Cell electrophysiology

2.5.1 The patch-clamp setup

The patch-clamp technique was initially developed to measure single ion channel currents (Neher and Sakmann, 1976). To record these miniature currents, the patch-clamp setup requires mechanical stability as well as shielding from electrical interference. The setup in this study was shielded by a Faraday cage (manufactured in the workshop of the MPI for Biophysical Chemistry), contained an anti-vibration table on pneumatic supports (TMC), an upright light microscope (Bx5b, Olympus, Japan), video camera for visualization, a piezoelectric micromanipulator (Tritor, Piezosysteme, Jena, Germany), an EPC 9 amplifier

(HEKA electronics, Germany), a MCPU-3 pump (Lorenz Messgerätebau, Germany), a perfusion system, and a monitor.

2.5.2 The patch-clamp of inner hair cells

Under microscopic control the patch pipette (with positive pressure of ~4-7 cm H₂O to prevent contamination of the pipette tip) was approached to the basolateral surface of a cleaned IHC. The Giga-Ohm seal was achieved by changing the positive pressure to light suction. Upon establishment of the on-cell configuration, the pipette capacitance (C_p) was compensated. The standard whole-cell configuration was then obtained by rupturing the patch beneath the pipette tip with a strong pulse of suction (see equivalent circuit in Fig. 2a). Compared to the standard whole-cell patch-clamp, perforated patch recordings (Horn and Marty, 1988) allow less invasive, long lasting and stable measurements. Here, the electrical access to the cell's interior was gained using the polyene antibiotic Amphotericin B. This compound forms channels in cholesterol or ergosterol containing membranes, which are permeable to monovalent ions and therefore allows to measure membrane currents but preserves soluble cytosolic components of the cell. However, Amphotericin B inhibits the formation of the seals. It is, therefore, important to fill the pipette tip with an Amphotericin-free solution by dipping it into that solution for ~20 sec (Sakmann and Neher, 1995). The diffusion of Amphotericin B to the tip of the pipette and formation of the low-resistance access to the cell took about 10 min in most of my experiments on IHCs.

The patch pipettes of approximately 3-6 M Ω resistance were pulled from borosilicate glass and heat-polished in order to promote better seal formation. To diminish the noise by

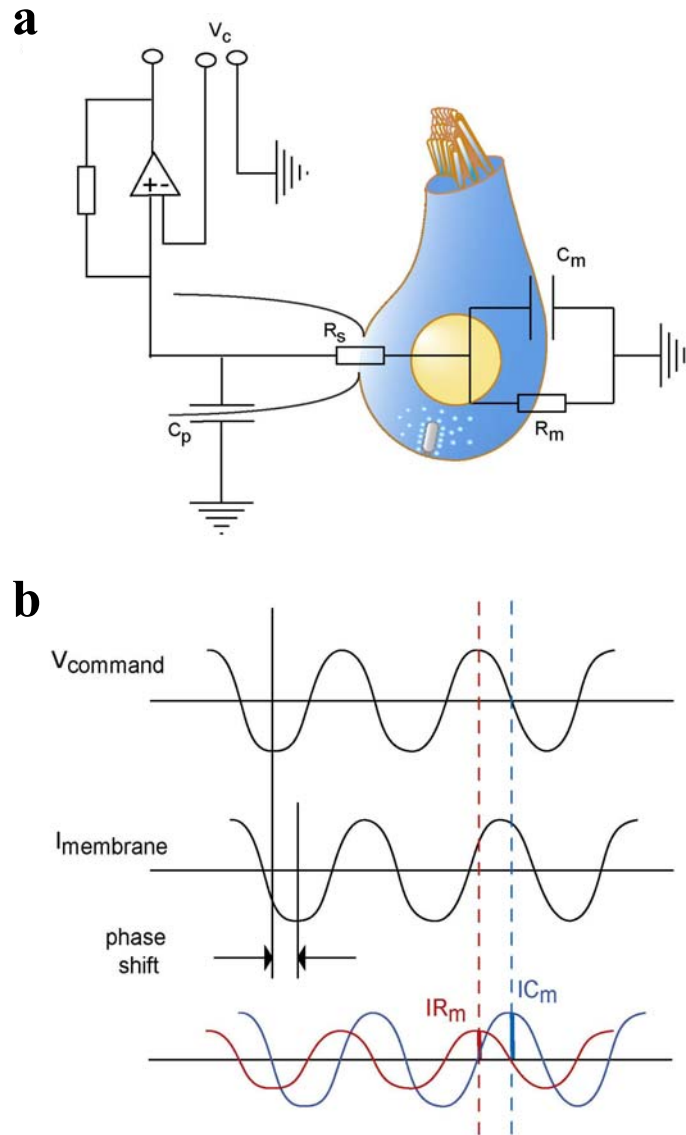


Figure 2. Patch clamp and Lindau-Neher technique. **a**, Equivalent electric circuit of the cell in the whole cell configuration. C_m - membrane capacitance, C_p - pipette capacitance, R_s - series resistance, R_m -membrane resistance, V_c - command potential. **b**, Using the Lindau-Neher technique we applied a sinusoidal voltage stimulus about a hyperpolarized potential and estimated cell capacitance from acquired magnitude and phase shift of the resulting current sinusoid.

reducing the pipettes capacitance the tips of the pipettes were coated with a hydrophobic silicone compound (G.E. Silicones, Netherlands) that was hardened in a hot air stream.

Materials and methods

The IHCs were voltage-clamped at -84 mV and stimulated by depolarizations of different durations to the peak Ca^{2+} current potential at intervals of 30 to 70 s, that was estimated before by probing the current-voltage relationship. EPC-9 amplifier (HEKA-electronics) controlled by Pulse software was used to low-pass filter and sample currents at 2-5 kHz and at 20-40 kHz, respectively. Table 1 summarizes the average passive electrical properties of the patched IHCs at the different postnatal ages. During experiments the preparation was continuously perfused with Ringer solution 0.3 ml/min at room temperature ($+22$ - 25°C).

	Number of patched IHCs	C_m (pF)	R_s ($\text{M}\Omega$)
8 weeks: WT (10 mM CaCl_2)	26	7.67 ± 0.3	21.56 ± 1.3
8 weeks: het (10 mM CaCl_2)	10	7.22 ± 0.6	17.56 ± 1.9
8 weeks: WT (2 mM CaCl_2)	7	9.26 ± 1.4	25.83 ± 2.2
8 weeks: MUT (10 mM CaCl_2)	24	7.35 ± 0.3	23.14 ± 1.3
3 weeks: WT (10 mM CaCl_2)	12	8.15 ± 0.5	20.49 ± 2.0
3 weeks: MUT (10 mM CaCl_2)	12	8.04 ± 0.4	22.84 ± 1.5
1 week: WT (10 mM CaCl_2)	9	7.51 ± 0.3	21.07 ± 1.6
1 week: MUT (10 mM CaCl_2)	9	6.88 ± 0.2	22.98 ± 1.8

Table 2. Cell capacitance (C_m) and series resistance (R_s) were repetitively estimated by time domain analysis of the cell's RC circuit during the perforated patch recording. C_m and R_s estimates were averaged throughout the experiment for each cell. The table presents the grand averages across the cells presented in Fig.3.7, 3.10, 3.13.

2.5.3 Capacitance measurements

In 1982 Neher and Marty reported that the patch-clamp technique combined with impedance analysis could be used to monitor membrane capacitance as a single cell assay of exocytosis. The cell membrane, a thin (~10 nm) insulating lipid bilayer with a transmembrane resting potential, functions as an excellent capacitor. Capacitance is proportional to the membrane area and is about 10 fF/ μm^2 for biological membranes. Exocytosis involves the fusion of the vesicle membrane with the plasma membrane. Since the cell capacitance is proportional to its surface area, any membrane added by exocytosis or removed by endocytosis is detected as a capacitance change (Fig. 2a, 2b). In the whole-cell configuration the technique can detect changes in capacitance in the order of a femto Farad, corresponding to the fusion of multiple vesicles.

We measured C_m using the Lindau–Neher technique (Lindau and Neher, 1988), implemented in the software lockin module of “Pulse” (sine + dc). A 1 kHz, 70 mV peak-to-peak sinusoid was applied about a DC holding potential of -84 mV (Fig. 2a, 2b).

2.5.4 Data analysis

Cells with a holding current exceeding -50 pA at -84 mV, R_s exceeding 25 M Ω for the whole cell recordings and R_s exceeding 35 M Ω for the perforated patch experiments were excluded from analysis. All voltages were corrected for liquid junction potentials. All currents were leak-corrected using a P/6-protocol. For K^+ - current measurements, R_s compensation was used (50–60%), and data were off-line corrected for the remaining voltage error. Setting the reversal potential used for software lock-in C_m estimation (values ranging

Materials and methods

from -35 to -65 mV) removed the rapid C_m transients, which were observed when an inappropriate reversal potential was entered into the C_m calculation.

All experimental data were analyzed using IgorPro software (Wavemetrics, Lake Oswego, OR). The membrane capacitance increments (ΔC_m) were estimated as the difference of the mean C_m after the end of the depolarization and the mean pre-pulse C_m (the initial 40 ms after the depolarization were skipped and the segments of 400 ms were averaged). Mean ΔC_m and Ca^{2+} current estimates present grand averages calculated from the mean estimates of individual IHCs. This avoided dominance of IHCs contributing more sweeps.

Means were expressed \pm sem and compared using Student's unpaired t-tests, with *, **, *** indicating $p < 0.05$, 0.02 and 0.01 , respectively.

2.6 Immunocytochemistry

2.6.1. Antibodies

The following antibodies were used in this study:

A mouse **anti-Bassoon Sap7f** (diluted 1:1000-1:500) generated against amino acids 756-1001 of the Bassoon protein (Gundelfinger laboratory, Magdeburg).

Guinea pig **anti-Piccolo** (1:1000) generated against amino acids 2172-2361 of Piccolo protein (Fenster et al., 2000; Gundelfinger laboratory, Magdeburg).

Rabbit **anti-calbindin D-28k** (1:100) serum against recombinant rat D-28k (Swant).

Anti-RIBEYE (1:1000-4000) rabbit antiserum (gift of H. Brandstaetter) against the A-domain of Ribeye.

Materials and methods

Anti-CtBP2 (1:100-200) mouse IgG1 (BD Biosciences) recognizes the B-domain of Ribeye and a transcription repressor CtBP2 (Schmitz et. al., 2000).

Rabbit **anti-glutamate receptors 2 & 3** (1:300- 1:1000) affinity purified polyclonal antibody (Chemicon).

Alexa Fluor 568 (1:200) goat anti-rabbit IgG (Molecular Probes).

Alexa Fluor 568 (1:200) goat anti-mouse IgG (Molecular Probes).

Alexa Fluor 488 (1:200) goat anti-mouse IgG (Molecular Probes).

Alexa Fluor 488 (1:200) goat anti-guinea pig IgG (Molecular Probes).

Alexa Fluor 633 (1:400) goat anti-rabbit IgG (Molecular Probes).

2.6.2. Buffers

120 mM Phosphate buffer contained: 100 mM Na₂HPO₄, 20 mM NaH₂PO₄.

GSDB (goat serum dilution buffer) contained: 16% normal goat serum, 450 mM NaCl, 0.3% Triton X-100, 20 mM phosphate buffer, pH 7.4

Fixative contained 4% paraformaldehyde (PFA) in 120 mM phosphate buffer.

Phosphate buffer solution (PBS) contained (in mM): 140 NaCl, 2.7 KCl, 8 Na₂HPO₄, and 1.5 KH₂PO₄.

Wash buffer contained: 450 mM NaCl, 20 mM phosphate buffer, 0.3% Triton X-100.

2.6.3. Immunostaining procedure

The freshly dissected apical parts of the organs of Corti were fixed with 4% PFA for 1 hour on ice. Thereafter the preparations were washed 3x10 min in PBS and incubated for 1 hour in GSDB in a wet chamber at room temperature. Primary antibodies were dissolved in

GSDB buffer and applied overnight at +4°C in a wet chamber. After washing with wash buffer (3x10 min) the whole mount Corti organs were incubated with secondary antibodies in GSDB in the wet light-protected chamber for 1 hour at room temperature. Then the preparations were washed 3x10 min in wash buffer and 1x10 min in 5 mM phosphate buffer, placed onto the glass microscope slides with a drop of fluorescence mounting medium (DakoCytomation) and covered by thin glass coverslips.

The immunostaining for 4Pi microscopy followed the same procedure using twice-higher concentrations of the primary antibodies.

2.6.4. Confocal microscopy

Confocal images were acquired using a laser scanning confocal microscope LSM 510 (Carl Zeiss Jena) with 488 (Ar), 543 (He-Ne) and 633 (He-Ne) lasers for excitation. We used 40X oil or water immersion objectives and the following band-path filters: BP 500-550, BP 565-615 and BP 650-710 nm. To acquire a three-dimensional image of the specimen a stack of two-dimensional images along the z-axis was taken with a step size 0.2 µm. The pixel size was 0.09 x 0.09 µm.

2.6.5. Data analysis

Images were processed using LSM 510 software (Carl Zeiss Jena). Whole mount preparations of the organ of Corti provided the possibility to analyze several IHCs in a row. Juxtaposition of the presynaptic ribbons with the postsynaptic boutons was investigated in 3D reconstructions of the organ of Corti and confirmed when there was no visually

Materials and methods

discernable space between the ribbon and the postsynapse in all three axes. In order to quantitatively investigate the immunofluorescence data in organs of Corti of Bassoon mutant and wild-type mice, the number of all ribbons, all postsynapses and overlapping ribbons were calculated by a blinded investigator and divided over a number of observed IHCs. The representative images were processed in Adobe Photoshop.

3. Results

3.1 Localization of Bassoon in the mouse organ of Corti

To determine the expression of synaptic proteins in the IHCs we performed immunostaining and confocal imaging on whole-mounts of the organs of Corti from 8-week-old mice. Similarly to the retinal ribbon synapses (Schmitz et al., 2000), RIBEYE was present at the ribbon synapses of IHCs (Fig. 3.1a). Antibodies against the RIBEYE A-domain and against the transcriptional repressor C-terminal binding protein 2 (CtBP2, which is transcribed from the same gene and only differs from the RIBEYE B-domain by 20 N-terminal amino-acids; Schmitz et al., 2000) produced a virtually identical staining pattern (Fig. 3.1a). In the following the latter antibody was used, because it stained both ribbons and nuclei and therefore allowed us to quantify the number of ribbon-containing synapses per IHC. The co-staining for RIBEYE and glutamate receptor 2/3 subunits (GluR2/3) revealed juxtaposed pairs of RIBEYE-marked ribbons and GluR2/3 spots of postsynaptic afferent fiber boutons (Fig. 3.1c). This is consistent with electronmicroscopic findings of a single ribbon per active zone and a single postsynaptic SGN bouton contacting each active zone of IHC in adult mice (Fig. 3.3a; Sobkowicz et al., 1986), see schematic representation in Fig. 3.1b.

Whereas Piccolo was found to be present at both photoreceptor and bipolar cell ribbons, Bassoon was expressed only in photoreceptor cell bodies (Dick et al., 2001) and no information was available about Piccolo expression at the hair cell afferent synapses. Staining by RIBEYE and Bassoon or Piccolo antibodies we first showed expression of these proteins in the IHCs. A number of Bassoon (Fig. 3.1d) and Piccolo (Fig. 3.1e)

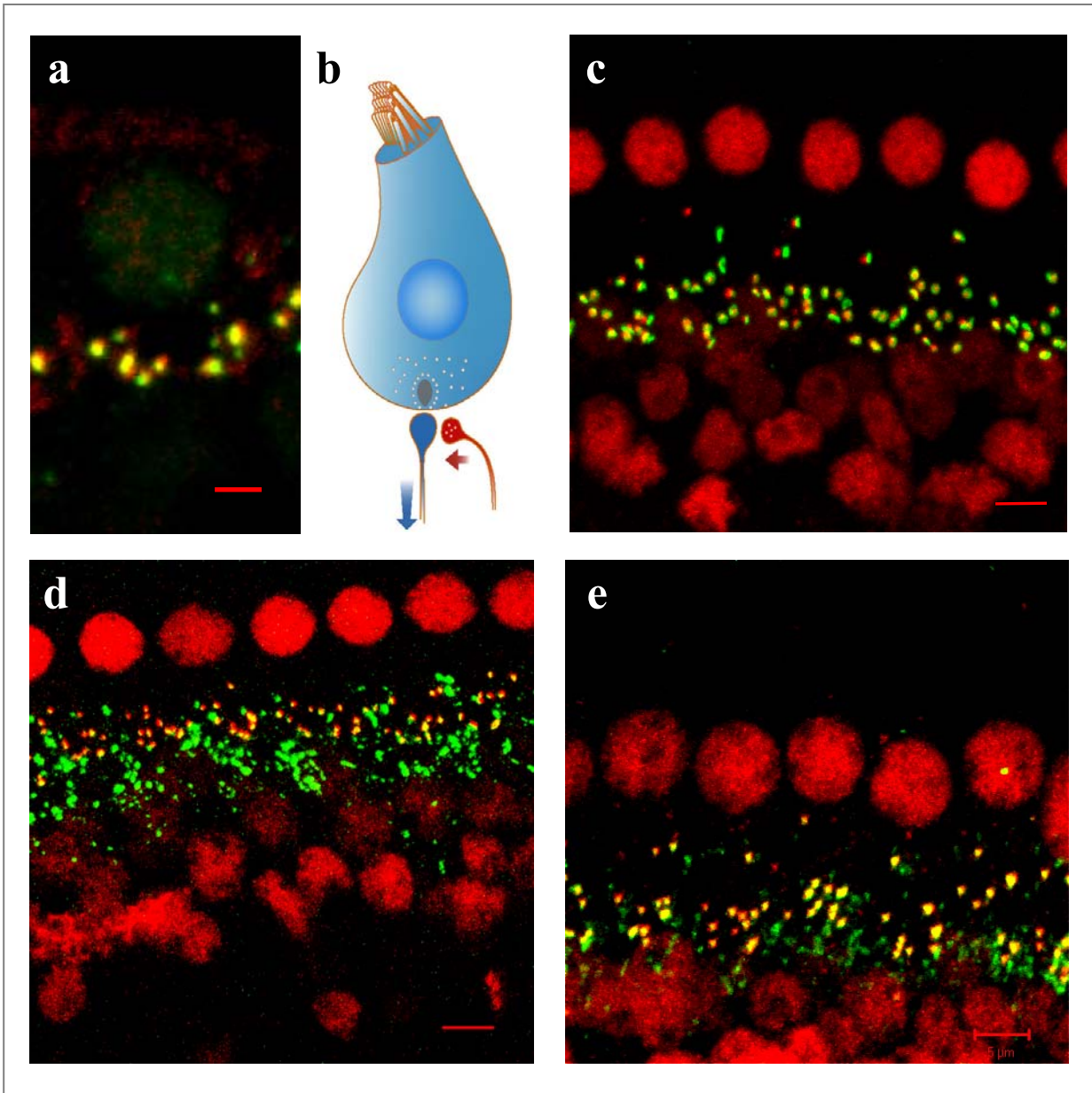


Figure 3.1. Proteins colocalized to IHC synaptic ribbons. **a**, Double staining of the organ of Corti for RIBEYE by a monoclonal antibody recognizing RIBEYE B-domain (green, raised against CtBP2) and a polyclonal antibody to RIBEYE A-domain (red): spot-like signals largely overlap in the overlay of confocal sections (scale bar: 2 μm). **b**, Schematic representation of an IHC, one exemplary afferent IHC synapse (blue) and one exemplary axodendritic synapse (red). Confocal stacks of the organ of Corti immunostained for RIBEYE B-domain (red) and GluR (**c**, green), Bassoon (**d**, green) or Piccolo (**e**, green), scale bar 5 μm .

Results

immunosignals overlapped with IHC ribbons. Some additional, non-overlapping Bassoon and Piccolo signals likely represented efferent nerve terminals innervating afferent dendrites (axodendritic synapses Fig. 3.1b, 3.3a).

3.2 Loss of Bassoon function in adult inner hair cells causes hearing impairment - synaptic audiopathy

3.2.1 Gross cochleae morphology of Bassoon mutants

Bassoon mutant mice have no abnormalities in brain architecture and no obvious morphological differences were detected at synapses of various brain regions (Altrock et al., 2003). We found a normal anatomical organization of the inner ear compartments (data not shown). At the transmission light microscopy level the basic structure of the mutant organ of

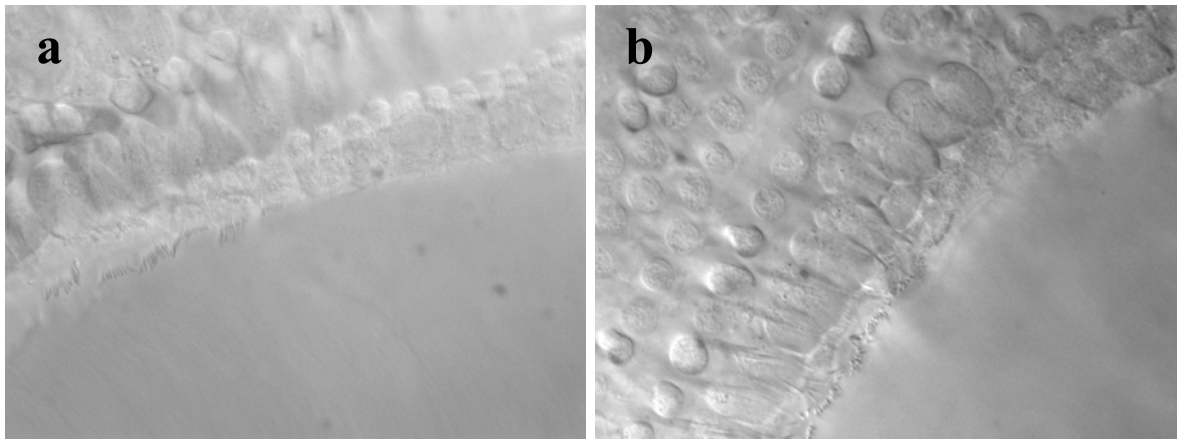


Figure 3.2. Gross cochlea morphology of the organ of Corti. Gradient contrast enhanced transillumination images taken with a CCD camera of the wild-type (a) and Bassoon mutant (b) organs of Corti. In the single row of the IHCs the stereocilia are arranged linearly in both mice. The preparations were not entirely flat, therefore IHCs were imaged at different levels. The mutant OHCs are present in three rows and displayed no abnormalities. The age of animals is p60.

Corti was comparable to that of wild-type littermates (Fig. 3.2). No major differences of hair cell stereocilia and somata were apparent (Fig. 3.2).

3.2.2 Ultrastructural changes in the IHCs of Bassoon mutants

3.2.2.1 IHCs at electron microscopy level

In collaboration with R. Pujol we explored Bassoon mutant morphology using electron microscopy. Cochleae were harvested, fixed and osmium-stained by cochlear perfusion in the Inner Ear lab and then embedded, cut and imaged by R. Pujol in Montpellier.

Figure 3.3b displays a representative synapse of an 8-week-old WT IHC. The ovoid electron dense ribbon tethered a halo of synaptic vesicles and was attached to the presynaptic density. The representative IHC synapse of a mutant littermate (Fig. 3.3c) maintained pre- and postsynaptic densities but lacked the ribbon. However, ribbon-deficient synapses of Bassoon mutant mice possessed ordinary docked synaptic vesicles at the active zones (Fig. 3.3f). Despite the lack of an anchored ribbon, some ribbons were found freely floating in the cytosol (Fig. 3.3c-d). Table 3 presents a quantification of electron microscopy data on ultrathin sections from 7 WT (WT_{EM}) and 6 mutant (MUT_{EM}) cochleae. Counting revealed a strong reduction of ribbon-containing synapses. We suspect that we underestimated the number of anchored ribbons in both genotypes mainly because, depending on its orientation with respect to the cutting axis, the ribbon may span only a single section and the series of thin sections was often not complete.

The active zone of the mutant synapses was usually occupied by tubular and cisternal membrane profiles (Fig. 3.3c-e). These profiles were reminiscent of the large endosomal membrane compartments previously described in ribbon synapses following depolarisation

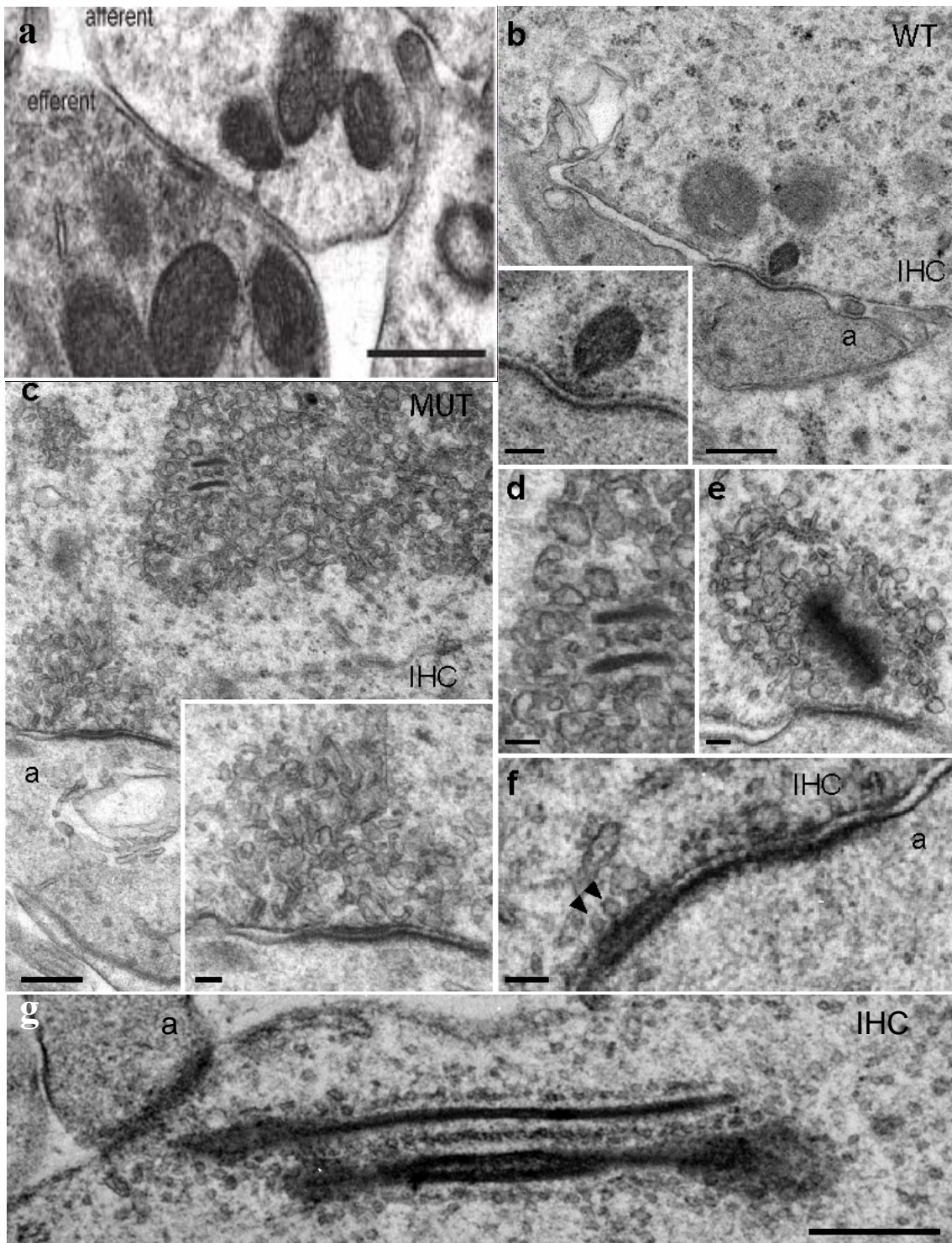


Figure 3.3. Electron microscopy: Bassoon anchors synaptic ribbons at IHC active zones. a, Electron micrograph of an efferent axodendritic synapse obtained from a WT organ of Corti; efferent: presynaptic terminal containing synaptic vesicles, afferent: dendritic ending on an IHC. Electronmicrographs of WT (b) and

Results

mutant (**c-g**) IHC ribbon synapses (**a**: afferent dendrite, insets: higher magnifications). **d**, Floating ribbons of (**c**) at higher magnification. **e**, “Medusa-like” ribbon of a mutant IHC. **f**, Mutant ribbon-deficient synapse with docked synaptic vesicles (arrow heads). **g**, Giant ribbons of a mutant IHC. All data were obtained on 8-week-old mice. Scale bars: 500 nm in (**a**), 400 nm in (**b, c, g**); 100 nm in (**d-f**) and insets (**b, c**).

(Paillart et al., 2003; Lenzi et al., 2002; Holt et al., 2003) and will be called “cisterns”, as in Lenzi et al., 2002. A pair of ribbons, embedded in another aggregate of cisterns, was found floating in the cytosol at some distance from the synapse (Fig. 3.3c, magnified in Fig. 3.3d). In some mutant IHCs we observed extremely long ribbons (Fig. 3.3g). Numerous cisternal aggregates were observed in IHCs from each of the 6 mutants analyzed, while only few isolated cisterns were found in a fraction (2/7) of WT animals. Membrane profiles resembled cisterns when distant from floating (Fig. 3.3d) or anchored ribbons (Fig. 3.3e), whereas they appeared vesicle-like when close to ribbons. Future experiments will have to determine the origin and nature of the cisterns in Bassoon-deficient IHCs.

Figure 3.3a illustrates an efferent axodendritic synapse obtained from a wild-type organ of Corti. Efferent axodendritic synapses were observed at comparable rates in mutant organs of Corti (data not shown).

In order to relate our synapse morphology to functional results we semiquantitatively analysed 42 WT and 20 mutant synapses in single ultrathin electron microscopy sections (Table 3). We conclude that the average ribbon of mature mouse IHC takes an ellipsoid shape. Only ribbons with a perpendicular orientation with respect to a sharply delimited postsynaptic density were analyzed. The maximal extensions along the vertical and horizontal axes were taken as height and ‘width’ estimates. Due to random 2D orientation of ribbons in the sections, ‘width’ estimates ranged between 25 and 354 nm (data not shown). For a rough approximation of ribbon surface from the electron microscopy data we averaged

Results

	WT _{EM}	MUT _{EM}	WT _{LM}	MUT _{LM}
num _{IHCs}	109	110	80	60
num _{afferent synapses}	250	210	909	701
fraction _{ribbon-containing synapses (%)}	42.4	0.4	91.3	12.4
length _{postsynaptic density (nm)}	746 ± 26 (n = 42)	823 ± 57 (n = 20)	-	-
height _{ribbon/4Pi RIBEYE spot (nm)}	230 ± 9 (n = 42)	-	255	-
length _{ribbon/4Pi RIBEYE spot (nm)}	278 ± 18 (n=9)	-	332	-
width _{ribbon/4Pi RIBEYE spot (nm)}	55 ± 8 (n=9)	-	200	-
num _{ribbon-associated SV in 2D}	14.2 ± 0.5 (n = 33)	-	-	-
num _{docked SV in 2D}	3.0 ± 0.2 (n = 33)	1.9 ± 0.3 (n = 18)	-	-
diameter _{SV (nm)}	30.0 ± 0.3 (n = 206, cv = 15.2)	27.8 ± 0.3 (n = 202, cv = 13.7)	-	-
distance _{ribbon-SV (nm)}	26.2 ± 0.6 (n = 195)	-	-	-
size _{small RIBEYE spots, 4Pi (nm)}	-	-	260 ± 4 (n = 201)	220 ± 20 (n = 15)
size _{big RIBEYE spots, 4Pi (nm)}	-	-	763 ± 12 (n = 38)	1273 ± 70 (n = 28)
surface (nm)	~2.38e ⁵	-	ellipsoid:~3.82e ⁵ sphere:~3.79e ⁵	-
num _{ribbon-associated SV 3D}	~125	-	ellipsoid:~203	-
num _{docked SV 3D}	~16	-	ellipsoid:~30	-
RRP _{synapse (vesicles/synapse) (conversion factor: ΔC_m/SV)}	53-64 _{ribbon-containing} (10) (28 aF)	~58 _{ribbon-contain.(1)} ~14 _{ribbon-deficient(11)} (24 aF)	-	-
RRP _{IHC (fF)}	15-18	5		

Table 3. Quantification of morphological results. Electron microscopy: the afferent IHC's synapses (num_{afferent synapses}) were identified as contacts of IHC (num_{IHCs}) and dendrite displaying pre- and postsynaptic densities in ultrathin sections from 7 WT and 6 mutant cochleae. The ribbon-associated synaptic vesicles were calculated as all vesicles within 30 nm distance from the ribbon, and docked vesicles that touched the plasma

Results

membrane. The 4Pi estimates of the three principal axes were obtained by approximating the major peak of the WT RIBEYE size distribution by a model that assumed an ellipsoid shape and random orientation of the ribbon with respect to the optical axis (Fig. 3.5e). The RRP of synaptic vesicles per synapse (RRP_{synapse}) was estimated from exocytic ΔC_m of Fig. 3.7, converted into vesicle numbers and related to the average number of synapse per IHC.

the lowest 20% of this distribution to yield an apparent width (“width_{ribbon}”) and the highest 20% groups for an apparent length (“length_{ribbon}”, Table 3).

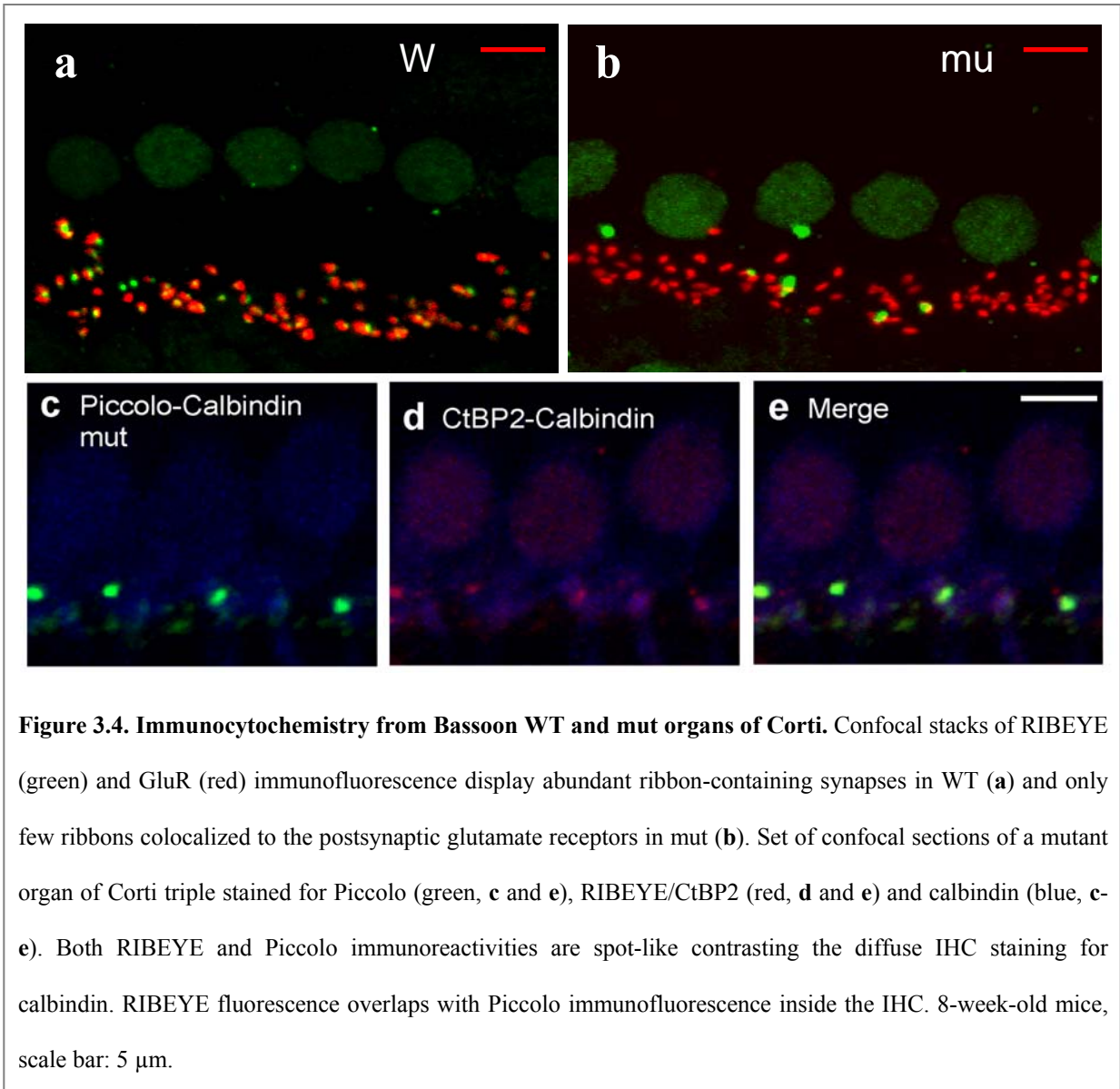
The number of ribbon-associated synaptic vesicles in 2D sections included all vesicles within 30 nm distance from the ribbon. Docked synaptic vesicles touched the presynaptic membrane and were dominated by ribbon-associated synaptic vesicles ($\sim 2/3$) in WT synapses. The total number of docked synaptic vesicles in EM was roughly approximated based on the 2D count of 3 docked synaptic vesicles, assuming a hexagonal packing with a 55% density along the ribbon’s length plus 3 synaptic vesicles at each end of the ribbon. Although we cannot rule out that our fixation paradigm caused transmitter release and subsequent synaptic vesicles depletion, we do not favour this hypothesis, because different from strongly stimulated ribbons (Lenzi et al., 1999; Lenzi et al., 2002) our WT IHC ribbons were densely populated with synaptic vesicles also at their base. In fact, our EM estimate of docked synaptic vesicles probably represents an upper estimate rather than an underestimate, since the 2D estimate of ribbon-associated synaptic vesicles lumped together slim and wide ribbon cross-sections. Synaptic vesicle diameters were measured from the lipid bilayer’s centres and synaptic vesicle capacitances were calculated assuming a specific membrane capacitance of $10 \text{ fF}/\mu\text{m}^2$ (Breckenridge and Almers, 1987). We did not correct for shrinkage due chemical fixation. Because of shrinkage we may have underestimated the vesicle size

and hence overestimated the number of docked and ribbon-associated vesicles. For a rough approximation of the number of ribbon-associated synaptic vesicles we calculated the surface around the ribbon that is available for vesicle packing based on EM shape estimates, the average distance of the vesicle from the ribbon ($\text{distance}_{\text{ribbon-SV}}$) and the outer synaptic vesicle radius (17.5 nm). We assumed hexagonal packing of synaptic vesicles (1039 nm² hexagons) within this surface at a density of 55% (Lenzi et al., 1999; Lenzi et al., 2002).

3.2.1.2 Analysis of “ribbon-containing” synapses with confocal microscopy

We compared morphological findings from Bassoon mutant and WT mice by confocal microscopy. Most of the IHCs WT synapses displayed juxtaposed RIBEYE and postsynaptic glutamate receptor immunoreactivities (Fig. 3.4a, 3.1c) and were defined as “ribbon-containing” synapses. On the contrary, mutant IHCs displayed low number of “ribbon-containing” synapses (Fig. 3.4b). The RIBEYE immunoreactivity that was not colocalized to the presynaptic regions probably represents floating ribbons shown by electron microscopy (Fig. 3.3c-f, 3.4b).

In our confocal analysis of 7 WT (WT_{LM}) and 5 mutant (MUT_{LM}) mice num_{IHCs} and $\text{num}_{\text{synapses}}$ represented the total counts of IHCs (visualized by CtBP2-positive nuclear staining) and afferent boutons (GluR immunofluorescent spots), respectively, which we observed in animated 3D reconstructions of the organs of Corti (Table 3). The number of RIBEYE-juxtaposed GluR spots was related to $\text{num}_{\text{synapses}}$ to yield the fraction of ribbon containing synapses. RIBEYE-juxtaposed GluR spots were identified, when we found signals to be in contact by visual inspection. Counting revealed a strong reduction of ribbon-



containing synapses in mutant IHCs, allowing 100% correct genotype prediction (Table 3). We captured many more synapses per investigated IHC and also obtained a much larger fraction of ribbon containing synapses in both WT and mutant IHCs in the confocal analysis when compared to electron microscopy. We suspect an overestimation of mutant ribbon-containing synapses due to insufficient lightmicroscopical separation of some close but not

synaptically related ribbon and GluR signals in our confocal analysis (e.g. floating ribbons of Fig. 3.3c).

In addition, we showed that floating synaptic ribbons in IHCs from Bassoon mutant mice contained RIBEYE (Fig. 3.4b-d) and Piccolo (Fig. 3.4c, e) proteins. Comparable with wild types, some Piccolo signals occurred in mutants outside the IHCs, most likely representing efferent presynaptic terminals forming axodendritic synapses with the afferent dendrites (Fig. 3.1e and Fig. 3.4c, e).

3.2.2.3 Investigation of ribbon morphology

Together with A. Egner (Dept. Nanobiophotonics, MPI for Biophysical Chemistry) we utilized the high axial resolution of multifocal 4Pi microscopy (Hell and Stelzer 1992; Egner et al., 2002) to estimate the ribbon size from large samples of WT and mutant RIBEYE immunofluorescent spots. Deconvolved 3D-reconstructions of RIBEYE- and GluR-labeled afferent synapses showed that both signals were closely juxtaposed in WT IHCs (Fig. 3.5a). In line with the electron microscopy data, mutant IHCs mainly displayed ribbon-deficient synapses (isolated postsynaptic spots in Fig. 3.5b). As illustrated in the representative 3D-reconstructions of IHC RIBEYE/CtBP2 immunofluorescence (Fig. 3.5c,d), WT IHCs showed many sub-micron RIBEYE spots, whereas mutant IHCs displayed far fewer, and mainly (65%) larger, RIBEYE-positive spots. The estimates of ribbon size obtained from mutant and WT RIBEYE spots, as described in Khimich et al., 2005 are plotted in figure 3.5e. The size distribution of WT ribbons displayed a major peak at 260 nm. It was approximated by a model that assumed an ellipsoid shape of the average WT ribbon and a random orientation of the ribbon with respect to the optical axis. This yielded estimates of its

Results

three principal axes of 201, 255 and 332 nm (red line in Fig. 3.5e, Table 3). The large RIBEYE spots in mutant and WT IHCs likely corresponded to stacks of floating ribbons, as observed in electron microscopy (e.g. Fig. 3.3c).

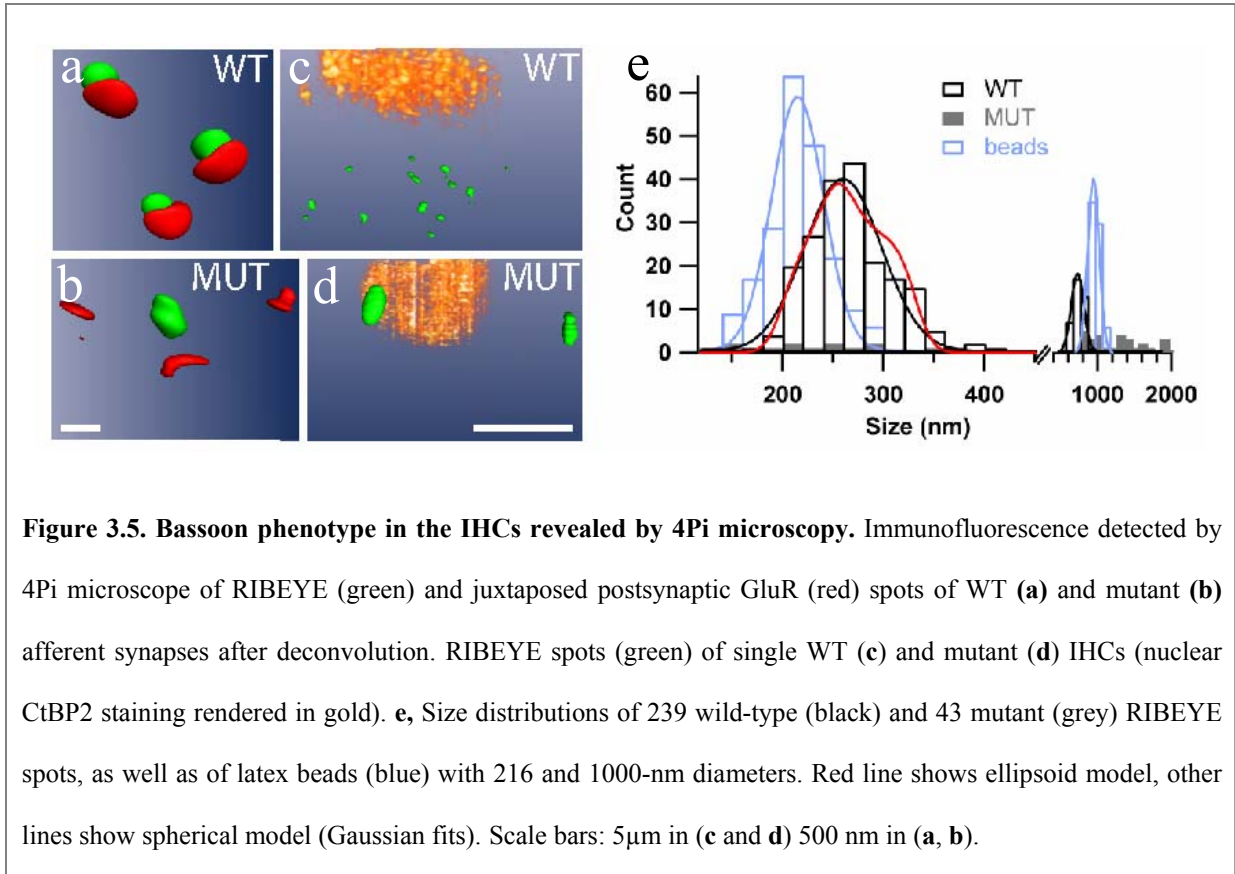


Figure 3.5. Bassoon phenotype in the IHCs revealed by 4Pi microscopy. Immunofluorescence detected by 4Pi microscope of RIBEYE (green) and juxtaposed postsynaptic GluR (red) spots of WT (a) and mutant (b) afferent synapses after deconvolution. RIBEYE spots (green) of single WT (c) and mutant (d) IHCs (nuclear CtBP2 staining rendered in gold). e, Size distributions of 239 wild-type (black) and 43 mutant (grey) RIBEYE spots, as well as of latex beads (blue) with 216 and 1000-nm diameters. Red line shows ellipsoid model, other lines show spherical model (Gaussian fits). Scale bars: 5 μ m in (c and d) 500 nm in (a, b).

3.2.3 IHC electrophysiology

3.2.3.1 Ca²⁺-current, exocytosis and endocytosis

During the following study we performed perforated-patch voltage-clamp measurements on IHCs of 8-week-old mice. The peak Ca²⁺ current amplitude of mutant IHCs was reduced by 36 % on average (Fig. 3.6b) but showed unchanged voltage dependence of activation (Fig. 3.6a). The Ca²⁺ current recorded from WT IHCs at 2 mM extracellular Ca²⁺ instead of usual

Results

10 mM, matched the Ca^{2+} current amplitude measured from mutants at 10 mM $[\text{Ca}^{2+}]_e$ (Fig. 3.6a). The shift of the current-voltage relationship of WT IHCs at 2 mM extracellular Ca^{2+} can be attributed to the reduced surface charge screening due to the decreased divalent ion concentration (Frankenhaeuser and Hodgkin, 1957). We favor the interpretation that the reduced Ca^{2+} current reflects a decreased number of synaptic $\text{Ca}_v1.3$ channels, although we

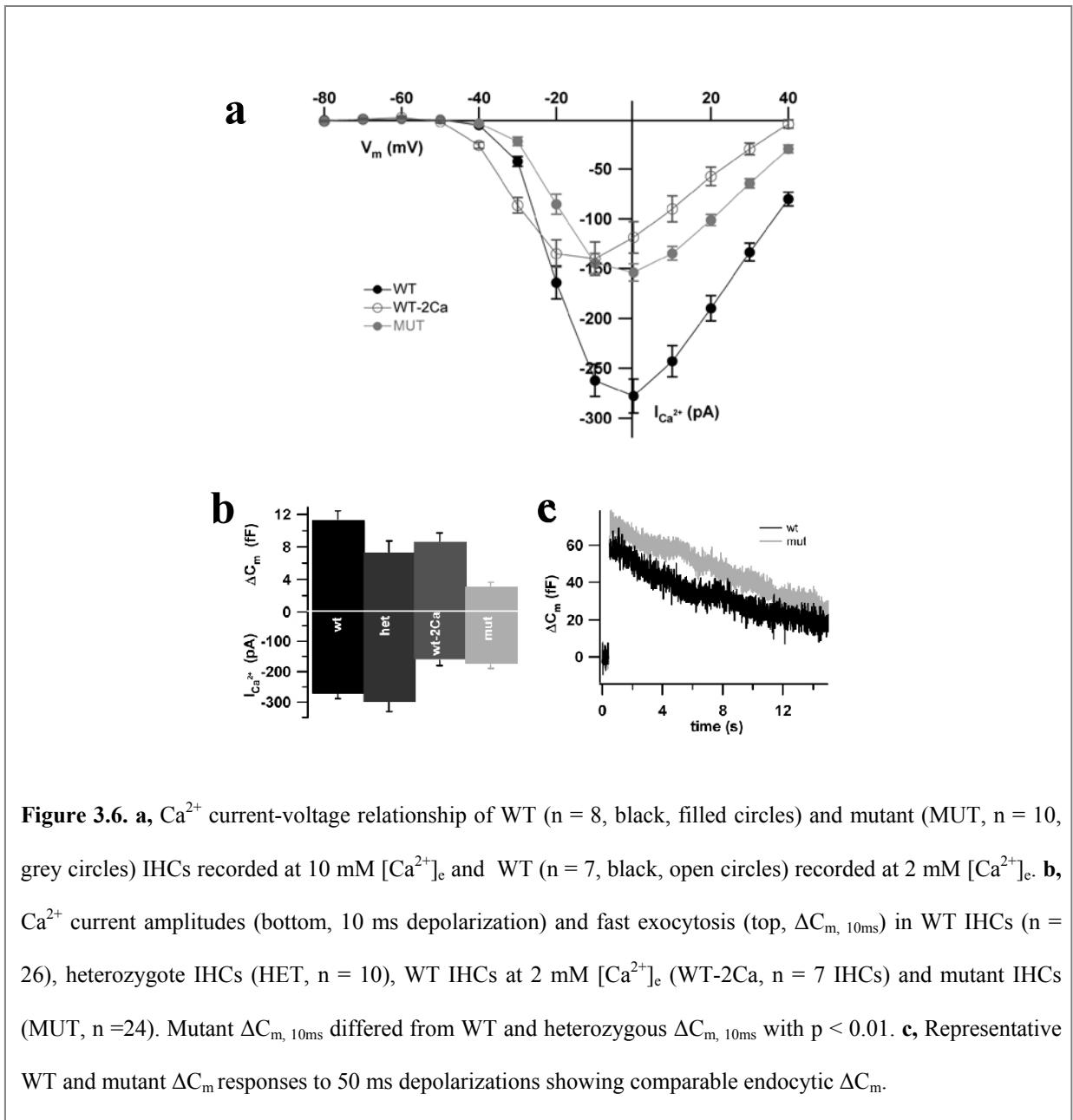


Figure 3.6. **a**, Ca^{2+} current-voltage relationship of WT ($n = 8$, black, filled circles) and mutant (MUT, $n = 10$, grey circles) IHCs recorded at 10 mM $[\text{Ca}^{2+}]_e$ and WT ($n = 7$, black, open circles) recorded at 2 mM $[\text{Ca}^{2+}]_e$. **b**, Ca^{2+} current amplitudes (bottom, 10 ms depolarization) and fast exocytosis (top, ΔC_m , 10ms) in WT IHCs ($n = 26$), heterozygote IHCs (HET, $n = 10$), WT IHCs at 2 mM $[\text{Ca}^{2+}]_e$ (WT-2Ca, $n = 7$ IHCs) and mutant IHCs (MUT, $n = 24$). Mutant ΔC_m , 10ms differed from WT and heterozygous ΔC_m , 10ms with $p < 0.01$. **c**, Representative WT and mutant ΔC_m responses to 50 ms depolarizations showing comparable endocytic ΔC_m .

Results

cannot rule out an impairment of $\text{Ca}_v1.3$ channel function in mut IHCs (e.g. open probability, conductance). Scaffolding by the ribbon or bassoon itself may be involved in stabilizing $\text{Ca}_v1.3$ channels at the active zone, thereby preventing excess degradation of channel protein.

Fast exocytosis, indicated by C_m increments in response to short stimuli (Moser and Beutner, 2000) was significantly reduced in the mutant IHCs as compared to WT or heterozygous littermates (Fig. 3.6b; for examples of Ca^{2+} currents and exocytosis for a single depolarization see Fig. 3.9e). We could not reproduce the mutant exocytic defect in WT IHCs when we reduced their Ca^{2+} current to the mutant level by decreasing the extracellular Ca^{2+} concentration from 10 to 2 mM (Fig. 3.6b). Therefore, the exocytic defect is most likely not primarily due to the reduced Ca^{2+} influx.

Next, we related membrane exocytic changes in large samples of mutant and normal IHCs to their synapse morphology to dissect ribbon-dependent exocytosis and the mechanism for the synaptic dysfunction. Although the resting IHC capacitance (C_m) and series resistance (R_s) were comparable in WT and mutant mice (Table 2), the mutant IHCs showed selective reduction of exocytosis for the short pulses (Fig. 3.7a). Exocytosis of 8-week-old WT IHCs was approximated by the sum of a small, fast secretory component and a large, slow component (Fig. 3.7a). We interpret the fastest discernible component ($\tau \sim 9$ ms) as exocytosis of the RRP (Neher, 1998). The total IHC RRP was estimated to ~ 18 fF or 640 synaptic vesicles by the model fit (conversion factor of 28 aF per synaptic vesicle, Table 3). Mutant exocytosis was subtracted to estimate the ‘ribbon-dependent’ RRP of ~ 15 fF or 530 synaptic vesicles (asterisks in Fig. 3.7a). Exocytosis of mutant IHCs could be better

Results

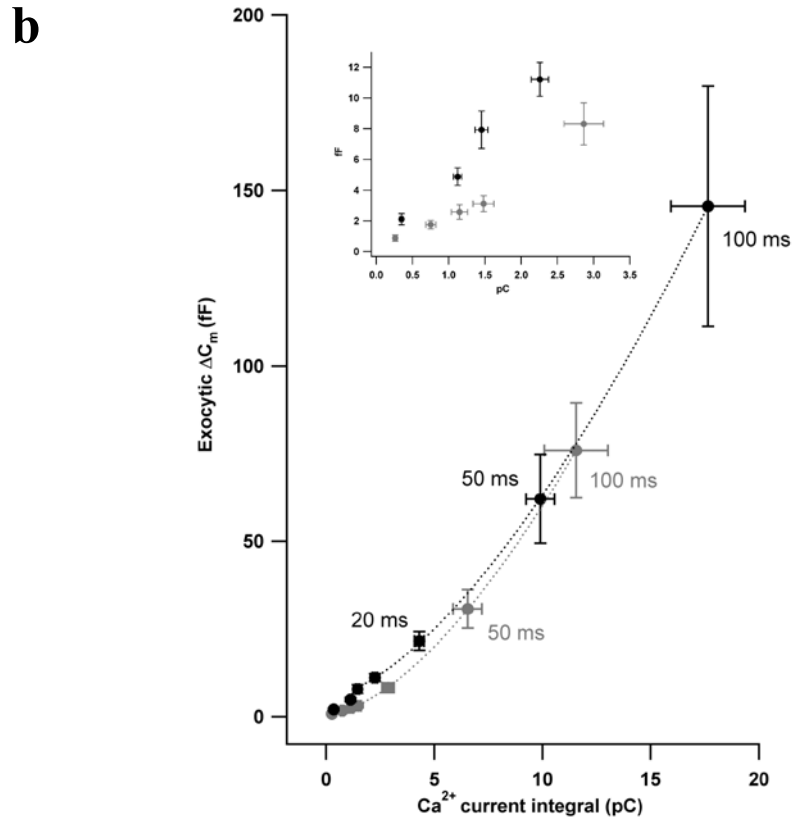
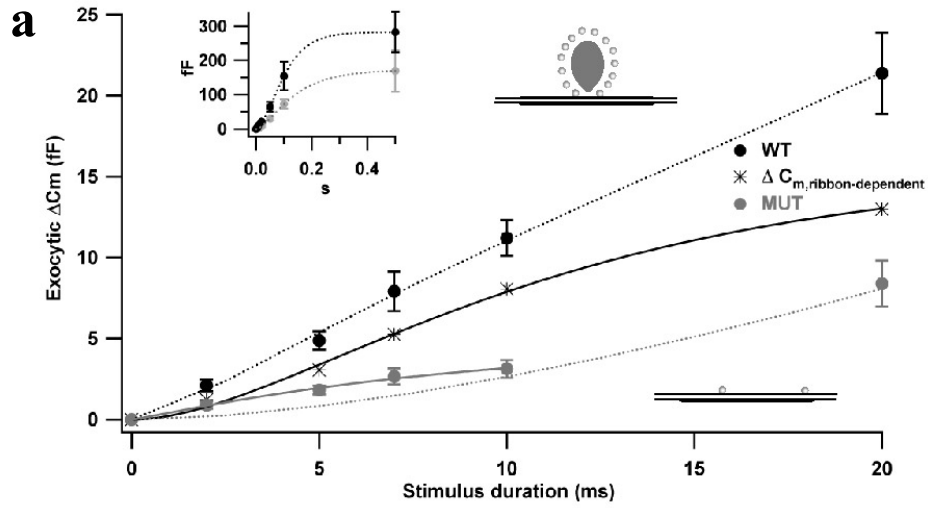


Figure 3.7. Dissection of ribbon-dependent hair cell exocytosis. a, Kinetics of exocytosis constructed from ΔC_m in response to depolarization of varying durations of WT (black circles, $n = 26$) and mutant (grey circles, $n = 24$) IHCs. Dotted lines are model fits to WT (black): $\Delta C_m = 18 \text{ fF} \times (1 - e^{-t/9\text{ms}})^{1.4} + 265 \text{ fF} \times (1 - e^{-t/64\text{ms}})^{2.8}$ and

Results

mutant (grey): $\Delta C_m = 172 \text{ fF} \times (1 - e^{-t/107\text{ms}})^{1.7}$. The inset shows the full range of data. The first 10 ms of mutant exocytosis were better approximated by $\Delta C_m = 5 \text{ fF} \times (1 - e^{-t/11\text{ms}})$, grey solid line. The difference of WT and mutant ΔC_m is represented by asterisks, approximated by $\Delta C_{m, \text{ribbon-dependent}} = 15 \text{ fF} \times (1 - e^{-t/8\text{ms}})^2$, (black solid line). WT and mutant ΔC_m differed with $p < 0.01$ for stimuli below 50 ms and with $p < 0.05$ for 50 ms, but were not significantly different for longer pulses. Cartoons illustrate typical 2D sections of WT (top) and mutant synapses (bottom). **b**, Plot of mean exocytic capacitance change (exocytic ΔC_m) of 26 WT and 24 mutant IHCs (8-week-old mice) vs. the corresponding Ca^{2+} current integral up to 100 ms of stimulation. Dotted lines: power functions were fitted to WT and mutant data, revealing comparable exponents (mutant: 1.5, WT: 1.6), fit range: 7-100 ms for both genotypes. Inset shows exocytic ΔC_m and Ca^{2+} current integrals in response to stimuli of up to 20 ms and 10 ms for mutant and WT IHCs, respectively.

approximated by using a single component model. However, some residual fast exocytosis ($\sim 5 \text{ fF}$ or 210 synaptic vesicles, conversion factor of 24 aF per synaptic vesicle, $\tau \sim 10 \text{ ms}$) was evident. This is consistent with the morphological finding of docked vesicles at the ~ 11 ribbon-deficient synapses and ~ 1 ribbon-containing synapse per mutant IHC (Fig. 3.3f, Table 3). Assuming that fast exocytosis exclusively represents synaptic transmitter release, each of the 10 ribbon-containing synapses of WT IHCs (9.8 ± 0.9 , $n = 7$ mice) on average holds a large RRP of 53-64 synaptic vesicles. This contrasts with a pool of ~ 14 synaptic vesicles at ribbon-deficient active zones (Table 3).

To show the genuine reduction of RRP, independent of the decreased Ca^{2+} current in Bassoon mutants, we plotted the mean exocytic capacitance change for different duration versus the corresponding Ca^{2+} current integral (Fig. 3.7b). We observed a reduction of fast exocytosis per unit of Ca^{2+} influx in mutant IHCs as compared to WT (inset of Fig. 3.7b), although the Ca^{2+} sensitivity of release appeared to be unchanged when considering sustained exocytosis.

Results

On the Figure 3.6c two representative examples obtained from WT and mutant IHCs illustrate similar capacitance increments for long depolarization pulse (50 ms) and comparable decline of capacitance trace within the next seconds, indicating normal membrane retrieval in ribbon-deficient IHCs.

3.2.3.2 BK K⁺ current

The potential consequence of the Bassoon inactivation on the Ca²⁺-activated K⁺ current in IHCs was examined in whole-cell patch-clamp experiments (in order to minimize R_s). To have the same Ca²⁺ influx (Fig. 3.6a, b), we used 10 mM and 2 mM CaCl₂ concentration in the extracellular saline for mutant and WT, respectively. To avoid contamination of the delayed rectifier and KCNQ4 potassium currents in our experiment, we applied short pulse

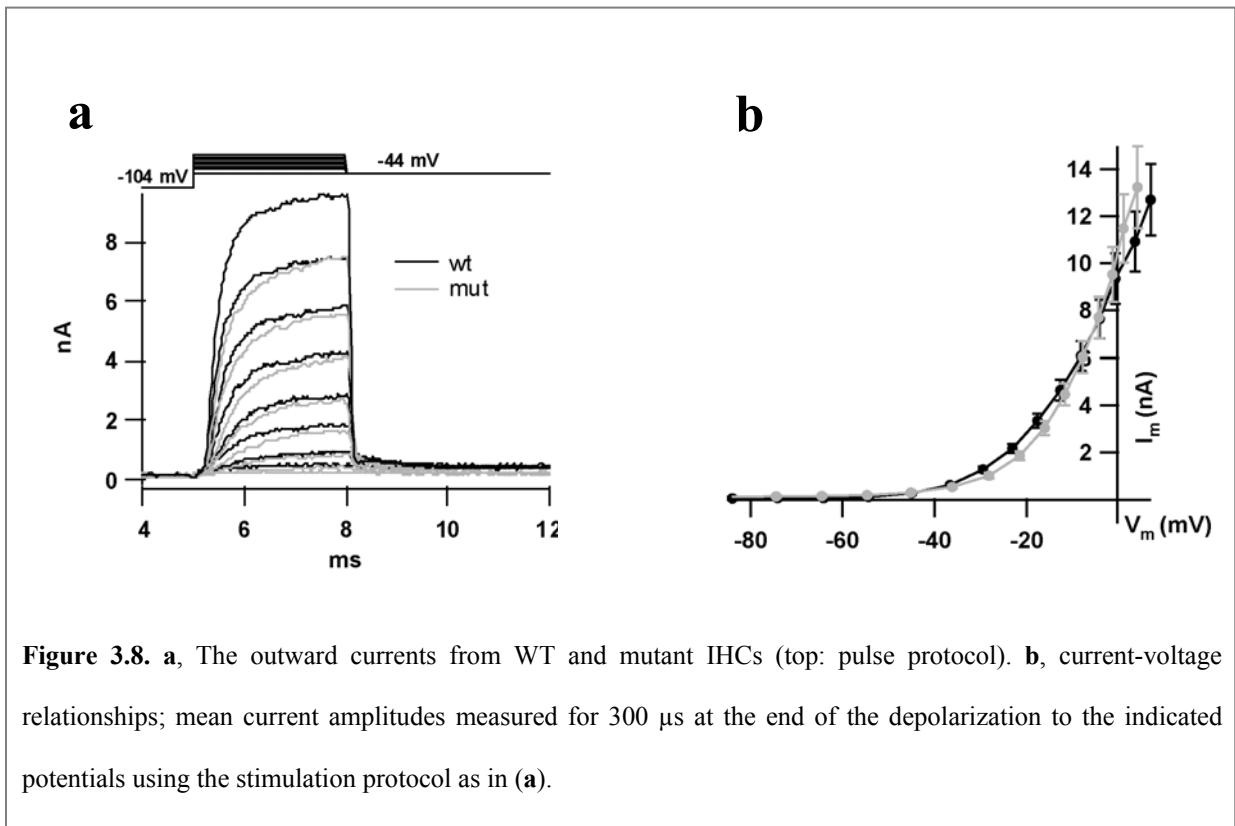


Figure 3.8. **a**, The outward currents from WT and mutant IHCs (top: pulse protocol). **b**, current-voltage relationships; mean current amplitudes measured for 300 μ s at the end of the depolarization to the indicated potentials using the stimulation protocol as in (a).

stimulation protocol (Fig. 3.8a; Oliver et al., 2003; Marcotti et al., 2004). Figure 3.8b displays the mean current amplitudes and shows no differences between WT and mutant animals. Thus, the Bassoon mutation and/or ribbon deficiency did not affect large conductance K^+ current amplitude.

3.2.4 Auditory morphophysiological correlation in Bassoon mutants

Taking advantage of the availability of different techniques in our laboratory, we performed a multi-step investigation in individual mice to rigorously test and correlate the consequences of IHC ribbon deficiency. Figure 3.9 documents the analysis for a representative pair of WT and mutant littermates. We started with recordings of auditory brainstem responses (*in vivo* system physiology was done by R. Nouvian in InnerEarLab) to clicks and short tone bursts (ABR, reflecting synchronized auditory pathway electrical activity, Fig. 3.9a, b), which revealed a distortion of the ABR waveforms and an increased auditory threshold in the mutant. The first ABR peak (I) was reduced and delayed also for suprathreshold stimuli reflecting an impaired SGN compound action potential in the mutant. To ensure that this reduction of synchronously activated SGNs was not due to a defect of active outer hair cell amplification we tested each animal for the presence of distortion product otoacoustic emissions (DPOAE; Kemp, 1978). Indeed, robust DPOAE were measured in both genotypes (Fig. 3.9c, d) except for 2 WT and 3 mutant mice (out of 17, data not shown) that were excluded because of uncertain OHC function. Thus, IHC ribbon-deficiency caused reduced neural output despite intact outer hair cell function, as confirmed by electrocochleography and otoacoustic emissions in additional experiments (Khimich et al., 2005). A combination of pathological ABR with intact otoacoustic emissions defines human

Results

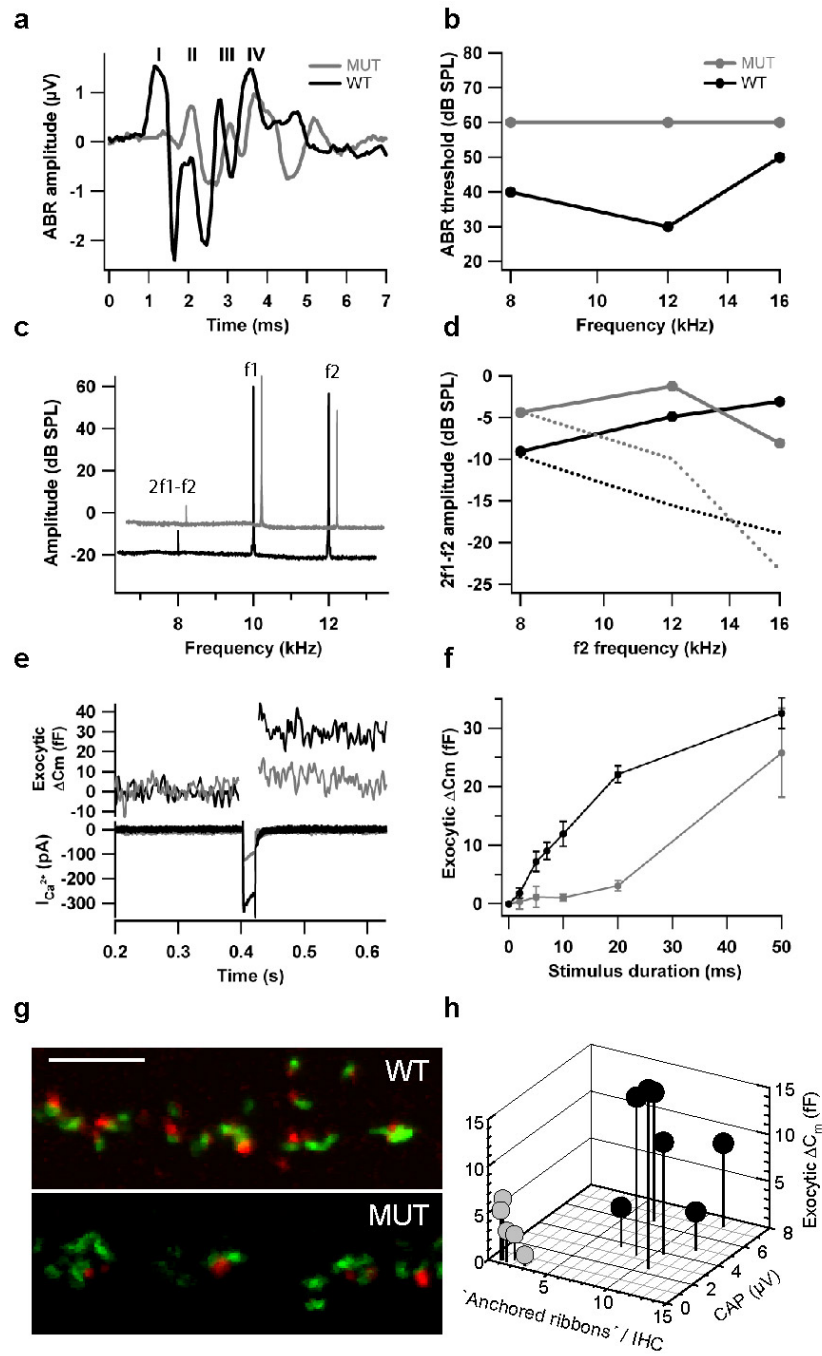


Figure 3.9. Synaptic ribbons are essential for fast exocytosis from hair cells and hearing. Analysis of a pair of mutant (grey) and WT (black) mice. **a**, ABR evoked by suprathreshold clicks (80 dB), peaks denominated by Roman numbers. **b**, ABR audiograms obtained by tone burst stimulation. **c**, Power spectrum of the microphone signal showing the $2f_1-f_2$ distortion product otoacoustic emission (DPOAE), as well as the primary tones (f_1

Results

and f2), mutant data slightly shifted for better visibility. **d**, DP-Gram, markers: 2f1-f2 DPOAE levels, dotted lines: noise floor around 2f1-f2. **e**, Representative Ca^{2+} currents and C_m changes recorded from WT and mutant IHCs (20 ms step depolarization). **f**, Kinetics of exocytosis constructed from ΔC_m of the same IHCs in response to depolarization of varying durations. WT and mutant ΔC_m differed significantly for 5, 10 and 20 ms depolarisations. **g**, Immunostaining for RIBEYE (red) and GluR (green) of IHC afferent synapses: single confocal sections through 4 neighboring IHCs. Scale bar: 5 μm . **h**, The diagram relates the mean number of synapse-anchored ribbons per IHC, fast exocytosis (ΔC_m in response to 10 ms depolarization) and CAP amplitude (approximated by ABR peak I amplitude) for individual mutant (grey) and WT (black) mice analyzed as in (**a-g**).

auditory neuropathy, a peripheral auditory disorder that is associated with poor speech discrimination. The cellular mechanisms of auditory neuropathy are not yet understood, but may involve defects of IHCs or SGNs (Starr et al., 1996).

Next, we performed a patch-clamp analysis of presynaptic IHC function using the same mice to test the hypothesis that synaptic dysfunction underlies their auditory neuropathy. In line with above-mentioned results, Figure 3.9e represents example traces of capacitance increments and Ca^{2+} currents for short depolarisation pulse. Figure 3.9f displays kinetics of IHC exocytosis for this pair of mice. The RRP was dramatically reduced in the mutant, whereas sustain secretion was not significantly different. The organs of Corti were then immunostained to count the number of ribbon-containing synapses (Fig. 3.9g), as introduced in Figure 3.4. A strong reduction of synapse-anchored ribbons was evident in the mutant. Both genotypes showed comparable numbers of postsynaptic spots. Table 3 summarizes the morphological findings. Figure 3.9h correlates the morphological and physiological results obtained from 5 mutant and 7 WT mice. In summary, the lack of synapse-anchored ribbons caused a reduction of fast exocytosis and synchronous synaptic activation of SGNs.

3.3 Bassoon inner ear phenotype during development

3.3.1 Auditory phenotype of Bassoon mutants at the onset of hearing

3.3.1.1 Synaptic organisation in IHCs of young hearing mice

To exclude a degeneration phenotype of Bassoon mutants, we also investigated 3-week-old mice, just after the onset of hearing. Similarly to 8-week-old animals, the co-staining of the organs of Corti for RIBEYE and GluR revealed juxtaposed organization of ribbons and postsynaptic glutamate receptors in the young WT (data not shown). The confocal images from 3-weeks mutant organs of Corti displayed a low number of “ribbon-containing” synapses and some “floating” ribbons in the IHC somata (data not shown). However, the quantification of the “ribbon-containing” synapses in young mice revealed larger numbers of synapse-anchored ribbons in both WT and mutant IHCs from 3-week-old mice in comparison with those from 8-week-old animals (Fig. 3.15). The reduction of anchored ribbons with age likely reflected developmental changes in the number of IHC ribbons shown by electron microscopy (Shnerson et al., 1981; Sobkowicz et al., 1982).

3.3.1.2 Cell electrophysiology in 3-week-old mice

3.3.1.2.1 Ca²⁺-current and exocytosis of the IHCs

The Ca²⁺ current from the IHCs undergoes developmental changes, as first has been reported by Beutner and Moser, 2000, and then confirmed by Brandt et al., 2003 and Johnson et al., 2005. It reached the maximal amplitude at postnatal day 6 and then gradually decreased until the onset of hearing. The peak Ca²⁺ current amplitude measured in perforated patch configuration from 3-week-old WT mice showed almost the same values as for the

Results

IHCs of 8-week-old animals (Fig. 3.15). The mutant IHCs at the age of 3 weeks revealed the same reduction of Ca^{2+} current amplitude as at 8 weeks (Fig. 3.15), arguing against a loss of Ca^{2+} channels due to age-dependent degeneration of the IHCs of Bassoon mutant mice after the onset of hearing.

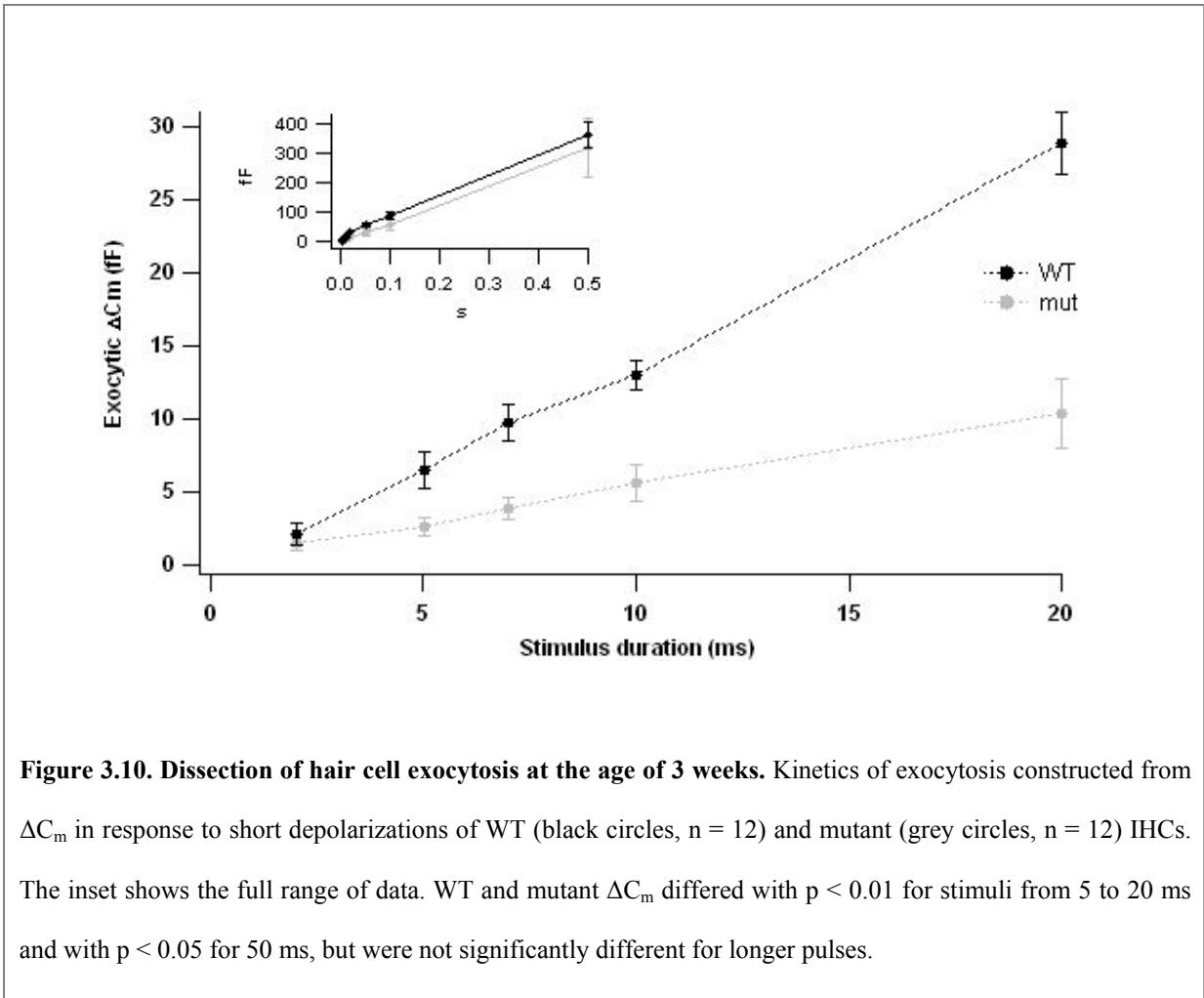


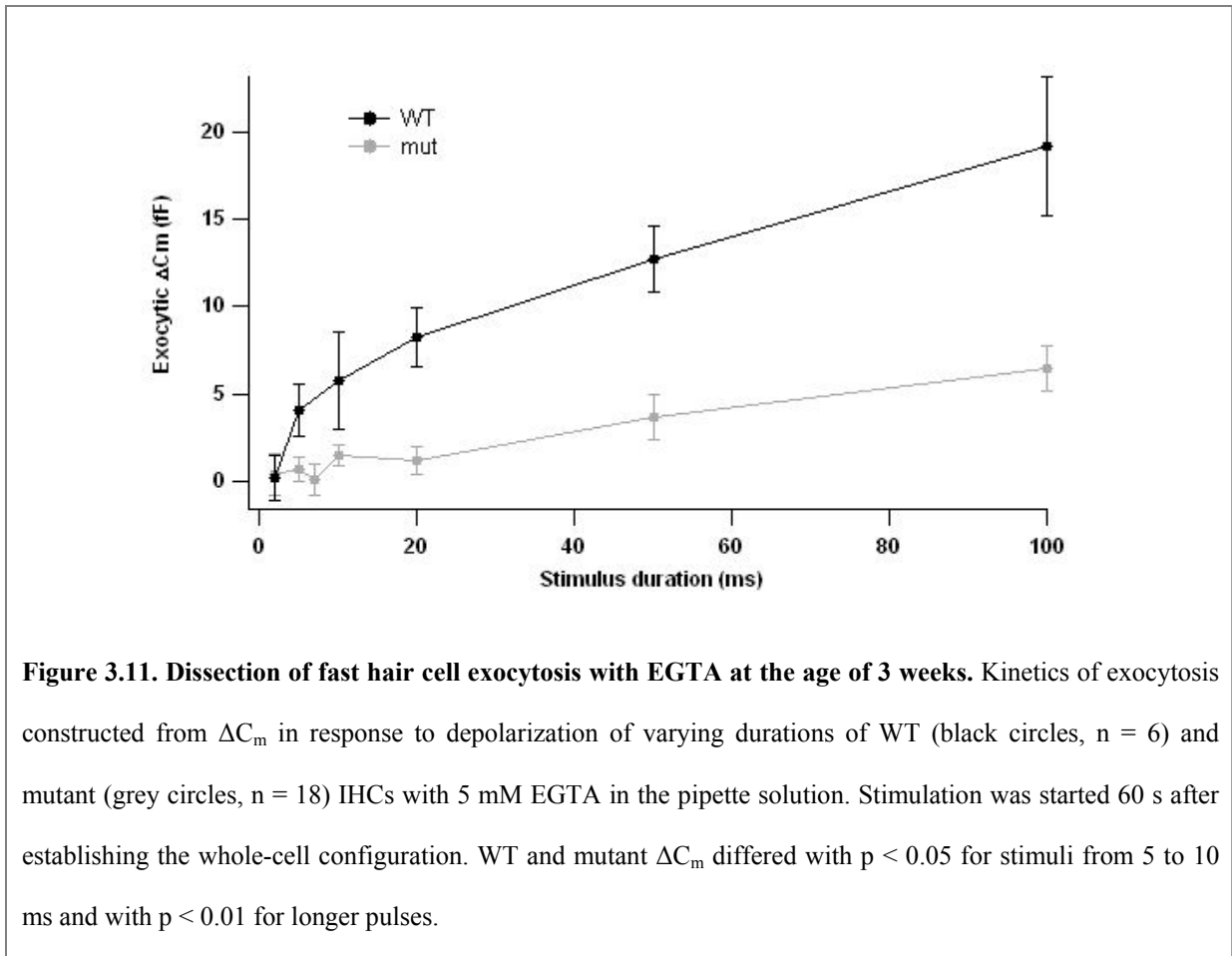
Figure 3.10. Dissection of hair cell exocytosis at the age of 3 weeks. Kinetics of exocytosis constructed from ΔC_m in response to short depolarizations of WT (black circles, $n = 12$) and mutant (grey circles, $n = 12$) IHCs. The inset shows the full range of data. WT and mutant ΔC_m differed with $p < 0.01$ for stimuli from 5 to 20 ms and with $p < 0.05$ for 50 ms, but were not significantly different for longer pulses.

The kinetics of exocytosis from the 3-week-old animals displayed a selective reduction of the RRP size in mutant IHCs when compared to WT littermates (Fig. 3.10), which was similar to the data obtained from 8-week-old mice. The slow component of exocytosis was not significantly different between the mutants and WT (inset of Fig. 3.10). The basal cell

Results

capacitance was comparable between both genotypes (Table 2). However, the amplitude of ΔC_m increments was larger for the young animal in comparison with the 8-week-old, which applies for both WT and mutants (Fig. 3.7a, 3.10, 3.15).

As has been shown before (Moser and Beutner, 2000), the IHC sustained secretory component can be strongly suppressed by applying a high concentration of slow Ca^{2+} chelator EGTA inside the cell. Here, we performed whole-cell patch clamp experiments on Bassoon mutant mice adding 5 mM EGTA to the intracellular solution. WT IHCs displayed fast exocytosis, but had a strongly inhibited slow secretory component (Fig. 3.11). The

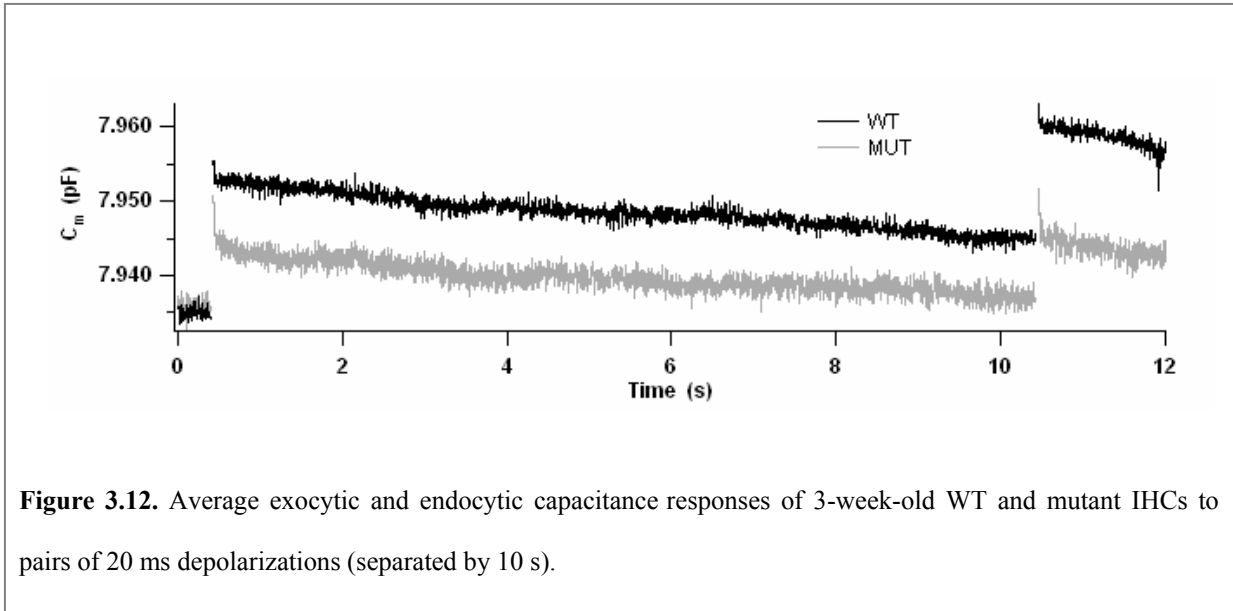


Results

exocytosis from mutant IHCs was dramatically reduced for both short and long stimuli, suggesting an impairment of RRP exocytosis. However, some residual fast exocytosis was evident in mutants (Fig. 3.11).

3.3.1.2.2 Endocytosis in young IHCs

The Figure 3.12 illustrates reduced capacitance increments for short depolarization pulses (20 ms) in mutant IHCs as compared to WT littermates and comparable decline of capacitance trace within the next seconds, indicating normal membrane retrieval in ribbon-deficient IHCs despite reduced RRP exocytosis.



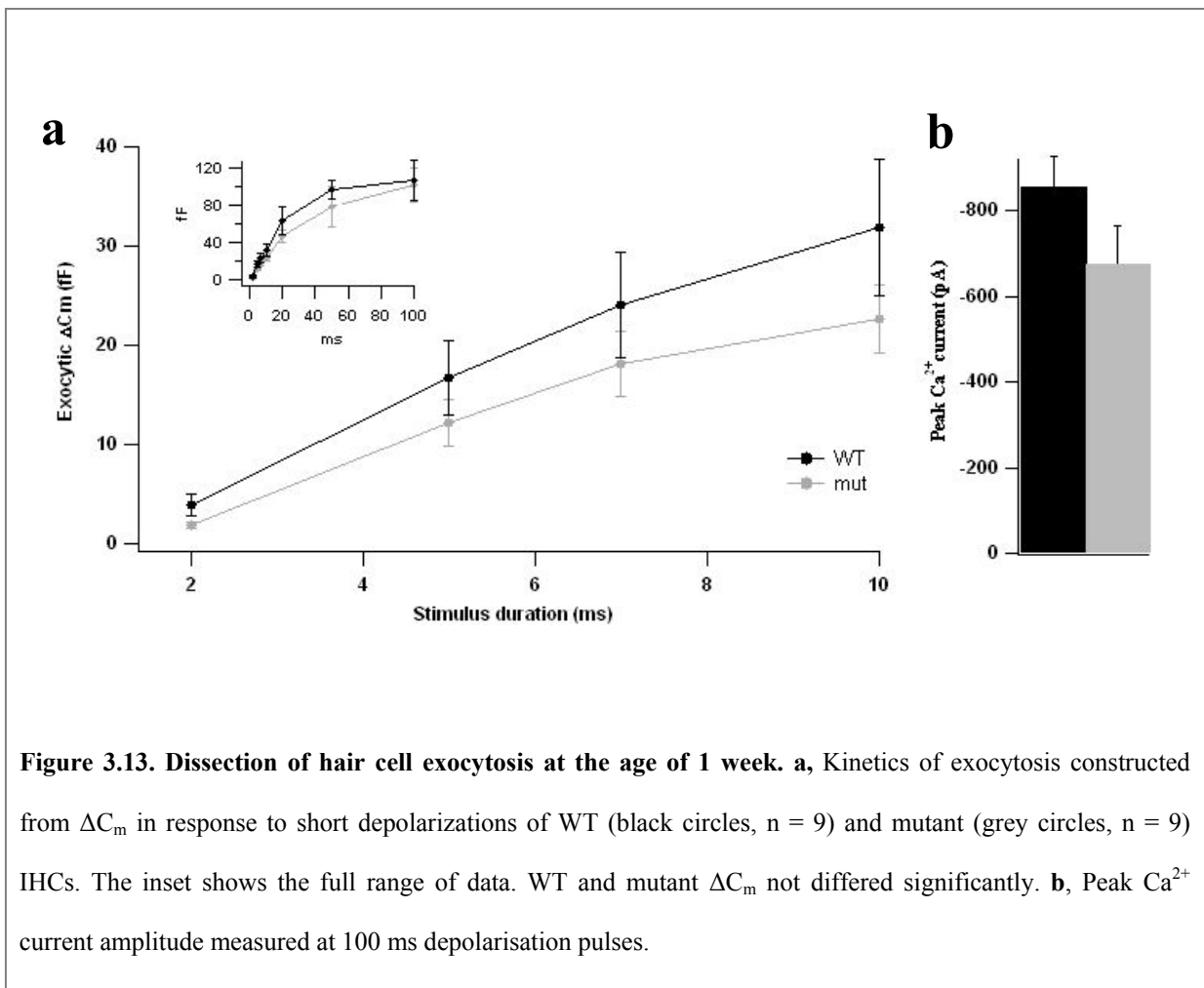
3.3.2 Analysis of Bassoon mutants before the onset of hearing

3.3.2.1 Patch clamp measurements of the IHCs

The kinetics of exocytosis from the 1-week-old animals (before the onset of hearing) displayed only a slight reduction of the RRP size in mutant IHCs in comparison with the WT

Results

littermates (Fig. 3.13a). Neither the slow component of exocytosis (inset of Fig. 3.10) nor the basal cell capacitances (Table 2) were significantly different between both genotypes. However, considering the huge Ca^{2+} currents at this age (Fig. 3.13b), it might be possible that even with a short stimulation we recruited the slow component of exocytosis (note the large ΔC_m increments from 1-week-old IHCs in comparison to the same stimulations in older mice). Alternatively, the multiribbon synaptic organization and immature Ca^{2+} buffer properties could also contribute to our observation.



Results

Indeed, when we applied 5 mM EGTA to the intracellular solution, limiting exocytosis to the subpopulation of vesicles localized close to Ca^{2+} channels, the WT ΔC_m increments were much smaller than in the perforated-patch recordings (Fig. 3.14, 3.13). However, WT IHCs displayed fast exocytosis, whereas mutant secretion was dramatically reduced, suggesting impairment of the RRP. Nevertheless, some residual fast exocytosis was evident in mutants (Fig. 3.14).

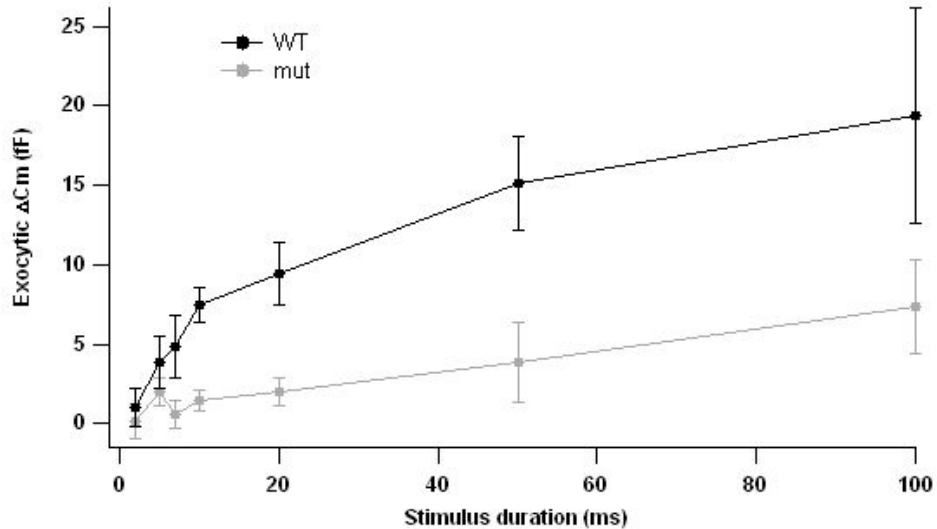


Figure 3.14. Dissection of fast hair cell exocytosis with EGTA at the age of 1 week. Kinetics of exocytosis constructed from ΔC_m in response to depolarization of varying durations of WT (black circles, $n = 26$) and mutant (grey circles, $n = 23$) IHCs with 5 mM EGTA in the pipette solution. Stimulation was started 60 s after establishing the whole-cell configuration. WT and mutant ΔC_m differed with $p < 0.01$ for stimuli from 10 to 50 ms and with $p < 0.05$ for 7 ms, but were not significantly different for other pulses.

3.4 Structure-function relationship of afferent wild type and mutant cochlear synapses during development

To prove that the lack of synapse-anchored ribbons caused a reduction of fast exocytosis and synchronous synaptic activation of SGNs we correlate morphological and physiological results from mutant and WT IHCs at different ages. We observed larger numbers of synapse-anchored ribbons in both WT and mutant IHCs of 3-week-old mice, which correlated with increased presynaptic IHC and postsynaptic SGN responses, compared to 8-week-old mice of the same genotype. The reduction of anchored ribbons likely reflected developmental changes in the number of IHC ribbons (Shnerson et al., 1981). Figure 3.15 correlates fast IHC exocytosis (membrane capacitance increments in response to 10 ms depolarization) and SGN compound action potential amplitudes with the number of synapse-anchored ribbons over all four groups. The lower panel of Fig. 3.15 displayed Ca^{2+} currents in mutant and WT IHCs from 8- and 3-week-old mice. Potentially, this impaired Ca^{2+} influx might contribute to the synaptic defect. However, Ca^{2+} currents were comparable between 3- and 8-week-old IHCs of each genotype, yet their synaptic functions differed. This argues for a genuine dependence of hair cell synaptic function on the presence of functional ribbons. Moreover, we did not observe the mutant exocytic phenotype when we reduced the Ca^{2+} current in 8-week-old WT IHCs to the mutant level by decreasing the extracellular Ca^{2+} concentration from 10 to 2 mM (asterisks in Figure 3.15). Together, these observations indicate that the synaptic dysfunction of Bassoon mutant mice was primarily due to the reduction of synapse-anchored IHC ribbons, rather than to the reduced Ca^{2+} influx or a general exocytic defect in the absence of functional Bassoon. This is consistent with a primary role of Bassoon in synaptic anchoring of ribbons (Dick et al., 2003).

Results

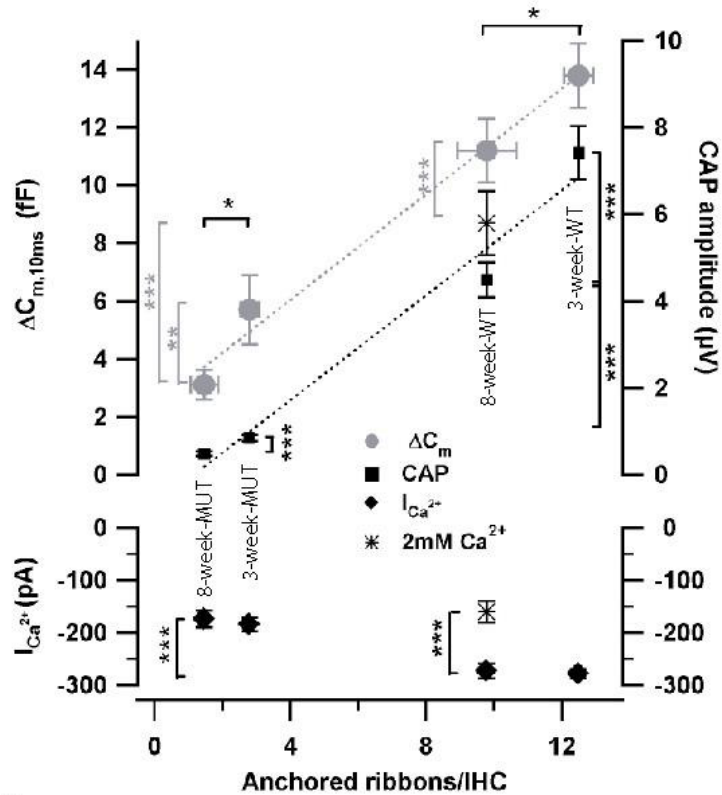


Figure 3.15. Fast exocytosis and compound action potential amplitude correlate with the number of anchored ribbons per IHCs during development. Mean ΔC_m (circles, upper panel, in response to 10 ms depolarization), corresponding peak Ca^{2+} currents (diamonds, lower panel) and ABR peak I amplitude (squares, upper panel, responses to 80 dB clicks) of 3- and 8-week-old WT and mutant mice were related to the numbers of synapse-anchored ribbons per IHC. ΔC_m and Ca^{2+} currents of 8-week-old WT IHCs were recorded at both 10 mM ($n = 25$ IHCs) and 2 mM extracellular Ca^{2+} (big asterisks, $n = 7$ IHCs). All other IHCs were recorded at 10 mM extracellular Ca^{2+} ($n = 24$ IHCs for 8-week-old mutant and $n = 12$ IHCs for both 3-week-old WT and mutant IHCs). ABR results were obtained from 28 and 21 ears of 8-week-old WT and mutant mice as well as from 14 and 6 ears of 3-week-old WT and mutant mice, respectively. Counting of synapse-anchored ribbons was based on 80 WT and 60 mutant IHCs of 8-week-old mice and on 78 WT and 94 mutant IHCs of 3-week-old mice. Dotted lines represent linear regressions (correlation coefficients > 0.95).

4. Discussion

4.1 Molecular anatomy of the hair cell ribbon synapse

The molecular components of the ribbon synapses have just recently begun to be investigated mainly in the retina. Only a couple of presynaptic proteins have been identified in the cochlear hair cells (Safieddine and Wenthold, 1999; Eybalin et al., 2002) and nothing was known about the molecular composition of IHC synaptic ribbon.

Piccolo and Bassoon are among the first CAZ (cytomatrix at the active zone) proteins to appear at nascent synapses in cultured neurons and they are components of an active zone precursor vesicle (Vardinon-Friedman et al., 2000; Zhai et al., 2001; Shapira et al., 2003). They are very large multidomain proteins intimately anchored to the cortical actin/spectrin cytoskeleton and present at both excitatory and inhibitory synapses in the brain (Richter et al., 1999; Wang et al., 1999; Fenster et al., 2000, 2003). This altogether makes Piccolo and Bassoon prime candidates for scaffolding proteins involved in the assembly of functional active zones. The synaptic ribbon is thought to be the equivalent of the CAZ of conventional synapses. It is defined and organized by a scaffold of proteins that are just beginning to be identified.

In the present study we first showed RIBEYE, Bassoon and Piccolo to be components of IHC ribbons (Fig. 3.1a, c-e). RIBEYE has self-aggregating properties and is a major constituent of the retinal ribbon (Schmitz et al., 2000; Zenisek et al., 2004). RIBEYE was also present in the floating ribbons in IHCs of Bassoon mutant mice (Fig. 3.4b). A recent study on the retina of Bassoon mutants revealed a twofold reduction of the overall amount of RIBEYE as compared to WT retina (tom Dieck et al., 2005). Bassoon interacts with the B-

Discussion

domain of RIBEYE by its 1653-2087 amino acid residues, which are missing in Bassoon mutant protein (tom Dieck et al., 2005). The residual 180 kDa Bassoon mutant protein was not targeted to the ribbons in photoreceptor terminals (Dick et al., 2003). Thus, the lack of Bassoon - RIBEYE interaction probably causes the defect in ribbon anchoring at the active zone of hair cells and photoreceptors (Fig. 3.3c, d; Dick et al., 2003).

Next, we showed Piccolo to be present in the mutant ribbons of the IHCs (Fig. 3.4c, e). Piccolo and Bassoon share regions of high sequence similarity (tom Dieck et al., 1998; Fenster et al., 2000). Both of them have been shown to bind to the identical region of CAST, a recently identified CAZ protein that forms a ternary complex with RIM1 and Munc13-1 in conventional synapses (Ohtsuka et al., 2002; Takao-Rikitsu et al., 2004). CAST is present at the active zone of photoreceptor ribbons (tom Dieck et al., 2005), but so far there are no data available about the expression of CAST in IHCs. Bassoon and Piccolo are the main components of Piccolo-Bassoon dense-core active zone precursor vesicles, shown in hippocampal neurons to carry active zone proteins, such as Bassoon, Piccolo, Syntaxin, RIM, Munc13, Munc18, SNAP25, Rab3a and N-type calcium channels (Zhai et al., 2001; Shapira et al., 2003). In the brain of Bassoon mutant mice Piccolo levels were increased 1.4-fold, suggesting a possibility of partial replacement of Bassoon function by upregulated levels of Piccolo (Altrock et al., 2003). A comparison with mice mutant for Piccolo and analysis of double mutants will be required to fully elucidate the molecular function of these two proteins in assembly and function of the active zone.

Interestingly, recent studies demonstrated that Bassoon through amino acid residues 1653-2087 is able to interact with the RIBEYE homologue CtBP1/BARS (C-terminal binding protein 1/ Brefeldin A adenosine diphosphate ribosylated substrate; tom Dieck et al., 2005).

Discussion

CtBP1/BARS, a protein that has previously been identified as transcriptional corepressor and Golgi-localized membrane-fission protein (Weigert et al., 1999; Turner and Crossley, 2001), is present both at photoreceptor ribbon synapses and at conventional synapses of retina and brain. Therefore, we might speculate on a role of CtBP1 in membrane fission events during endocytosis. As a reduction of CtBP1 was found in the CNS of Bassoon mutant, a recruitment of CtBP1 by Bassoon was discussed (tom Dieck et al., 2005). The IHCs from Bassoon mutants display plenty of aberrant tubular and cisternal, probably endosomal, membrane profiles at the electron microscopy level (Fig. 3.3c-e). One speculation is that the enzymatic activity of CtBP1 and perhaps CtBP2 may be required for vesicle fission from endosomal membrane in hair cells. The inactivation of Bassoon may cause a reduction of CtBP1 and CtBP2 also in IHCs. Therefore, testing the CtBP1/BARS expression in the IHCs and elucidation of its function could be the first step in understanding a potential enzymatic function of ribbon proteins in endocytosis. Our capacitance measurements from Bassoon mutant IHCs clearly demonstrated an intact endocytic membrane retrieval following exocytosis, arguing against the suggested role of CtBP1/CtBP2 in this process (tom Dieck et al., 2005).

4.2 Phenotype of Ca²⁺ and K⁺ currents in Bassoon mutants

The Ca²⁺ currents were reduced in the IHCs from 8-week-old mutant mice (Fig. 3.6b) but showed a normal voltage-dependence of activation (Fig. 3.6a). However, the same reduction (~35%) was observed at the age of 3 weeks (Fig. 3.15) and a significant decrease of Ca²⁺ current was already measured in 1-week-old animals (Fig. 3.13b). This argues against a loss of L-type Ca²⁺ channels in mutant IHCs accompanying some form of progressive

degeneration in hair cells, but might rather reflect insufficient recruitment and/or stabilization of $\text{Ca}_v1.3$ channels at the Bassoon-deficient active zone. Although preliminary experiments showed spot-like clustering of Ca^{2+} channels in WT IHCs (data not shown), future experiments are needed to rigorously test the distribution of Ca^{2+} channels in Bassoon mutants.

Despite the reduction of Ca^{2+} current we measured comparable amplitudes of BK K^+ current in WT and mutant IHCs (Fig. 3.8a, b). Hence, unlike in another synaptic disorder of hair cells (Cav 1.3 knockout), BK-channel expression is not affected in the Bassoon mutant. In contrast to previous assumptions of BK being close to Ca^{2+} channels and active zones, our recent immunocytochemistry data revealed BK localization at the apex of the IHC in both WT and Bassoon mutant mice (data not shown). Thus, although BK channels are Ca^{2+} activated K^+ channels, they are spatially separated and probably mainly voltage gated in the IHCs (Marcotti et al., 2004).

4.3 Mechanism of exocytosis at the IHC ribbon synapses – lessons from the Bassoon mutant

It is not clear how many synaptic vesicles undergo exocytosis at a single afferent synapse after a brief acoustic stimulus *in vivo*. Postsynaptic recordings from immature IHC afferent synapses showed that transmitter release from a single vesicle is sufficient to depolarize the SGN to threshold. Nonetheless, synchronized release of several vesicles occurs frequently (Glowatzki and Fuchs, 2002). Our data suggest that, indeed, synchronous auditory signaling relies on precisely timed release of several synaptic vesicles at the mature afferent IHC synapse, which in turn requires the presence of the ribbon. Parallel and synchronized release

Discussion

of multiple synaptic vesicles at the IHC ribbon synapse is probably required to reduce jitter of postsynaptic action potentials. The achieved precision of stimulus coding enables auditory brainstem neurons to detect sub-millisecond interaural time differences (Trussell, 1999). In contrast to large auditory brainstem synapses, such as the calyx of Held, where parallel transmitter release at multiple active zones ensures temporally precise excitation of a large neuronal soma, parallel and precisely timed release of multiple vesicles at one ribbon-containing hair cell active zone excites a very small postsynaptic terminal (Lieberman, 1982). Possible mechanisms include parallel fusion of docked synaptic vesicles and sequential fusion of more distal ribbon-associated vesicles to the membrane of previously fused proximal vesicles (Heidelberger et al., 1994). We favor the hypothesis that RRP exocytosis is dominated by fusion of docked vesicles (Zenisek et al., 2000; Fuchs et al., 2003; Lagnado, 2003; Sterling and Matthews, 2005), and that the ribbon positions synaptic vesicles close to Ca^{2+} channels to ensure efficient stimulus-secretion coupling.

However, recently it was suggested that fast exocytosis in hair cells may be mediated by vesicles that are not docked at active zones (Edmonds et al., 2004; Spassova et al., 2005). To test the idea that synaptic vesicles tethered to the ribbon far from the presynaptic membrane might contribute to fast IHC exocytosis, we compared the number of readily releasable synaptic vesicles to the numbers of docked and total ribbon-associated synaptic vesicles. Hence, the number of readily releasable synaptic vesicles (about 53-64 per synapse, Table 3) exceeded our estimate for the number of docked synaptic vesicles (16-30 per synapse, Table 3), suggesting that remote tethered synaptic vesicles might contribute to fast IHC exocytosis. Nevertheless, it remains possible that we underestimated the number of docked synaptic

Discussion

vesicles e. g. due to chemical fixation (Smith and Reese, 1980) and that the RRP entirely consists of docked synaptic vesicles in mouse IHCs.

Potentially, the impaired Ca^{2+} influx might contribute to the synaptic defect. Our hypothesis that synaptic defect is primarily due to the lack of the ribbon, which potentially acts as a positioning device, is supported by four observations. First, we observed larger numbers of synapse-anchored ribbons in both WT and mutant IHCs of 3-week-old mice (just after the onset of hearing), which correlated with increased presynaptic IHC and postsynaptic SGN responses, compared to 8-week-old mice of the same genotype (Fig. 3.15). The reduction of anchored ribbons likely reflected developmental changes in the number of IHC ribbons (Shnerson et al., 1981). Ca^{2+} currents were comparable between 3- and 8-week-old IHCs of each genotype, yet their synaptic functions differed (Fig. 3.15). This argues for a genuine dependence of hair cell synaptic function on the presence of functional ribbons. Secondly, we did not observe the mutant exocytic phenotype when we reduced the Ca^{2+} current in 8-week-old WT IHCs to the mutant level by decreasing the extracellular Ca^{2+} concentration from 10 to 2 mM (Fig. 3.6b, 3.15). Thirdly, we observed a reduction of fast exocytosis per unit of Ca^{2+} influx in mutant IHCs, although the Ca^{2+} sensitivity of release appeared to be unchanged when considering sustained exocytosis (Fig. 3.7b). Mutant IHCs showed robust sustained exocytosis (Fig. 3.7a, 3.10) and endocytic membrane retrieval (Fig. 3.6b, 3.12). Together, these observations indicate that the synaptic dysfunction of Bassoon mutant mice was primarily due to the reduction of synapse-anchored IHC ribbons, rather than to the reduced Ca^{2+} influx or a general exocytic defect in the absence of functional Bassoon. This is consistent with a primary role of Bassoon in synaptic anchoring of ribbons (Dick et al.,

2003). Finally, the EGTA experiments indicate a severe defect of Ca^{2+} channel – release site coupling.

Due to the developmental changes of glutamate receptor expression in type I afferent fibres (Eybalin et al., 2004), so far we could not obtain high quality immunostaining of postsynapses or quantify IHCs anchored ribbons from 1-week-old mice.

Whereas the above results highlight the ribbon's function in synchronous synaptic transmission, the role of the ribbon in sustained exocytosis is less clear. The finding of robust sustained exocytosis in mutant IHCs (inset Fig. 3.7, 3.10, 3.13) is surprising in the light of the previously suggested “conveyor belt” model of the ribbon (Fuchs et al., 2003; Lagnado, 2003; Sterling and Matthews, 2005). It suggests that slow exocytosis occurs at ribbon-deficient synapses and additional fusion outside the active zone contributes (Moser and Beutner, 2000; Zenisek et al., 2000; Beutner et al., 2001). Indeed, the Bassoon mutants were not completely deaf, indicating that the remaining fast exocytosis and the presence of slow exocytosis support some residual auditory signaling, but are unable to provide temporally precise sound coding. Future studies should address this hypothesis by recording the responses of single spiral ganglion neurons.

4.4 Bassoon mutants – a mouse model for synaptic audiopathy

Although unlikely, a dominant-negative effect of $\text{BSN}\Delta\text{Ex4/5}$ cannot be completely ruled out. Consistent with a loss-of-function effect of the $\text{BSN}\Delta\text{Ex4/5}$ mutation, heterozygous animals have quite normal audiograms and IHC synaptic morphophysiology (Fig. 3.6b and data not shown).

Discussion

Whereas Bassoon is expressed in the lateral efferent fibres, synaptic function of the efferent boutons and their influence on the auditory phenotype remains to be investigated. One of the experiments would be to measure the postsynaptic cholinergic currents in immature mutant IHCs. In order to investigate the IHC synaptic functions in future experiments we are planning to explore the ribbon-deficient IHCs with total internal reflection microscopy and establish the double-patch of the IHCs and postsynaptic boutons in our laboratory.

So far, no human hereditary deafness has been reported to result from a Bassoon mutation. However, this mouse model of synaptic audiopathy has an increased hearing threshold and impaired temporally precise sound coding. A defect of synchronous IHC synaptic transmission could present a pathomechanism of human auditory neuropathy and explain the poor speech discrimination that is observed. Testing for a potential defect in sound localization remains an important task. Further genetic analysis of hearing-impaired families will be required to explore whether mutations in the gene coding for Bassoon cause human synaptic audiopathy.

5. Summary

During this work we investigated organization, molecular composition and function of hair cell ribbon synapses. We demonstrated RIBEYE, Bassoon and Piccolo to be components of IHC synaptic ribbons.

In the present study we showed that anchoring of IHC ribbons is impaired in mouse mutants for the presynaptic scaffolding protein Bassoon. The lack of active, zone-anchored synaptic ribbons reduced the presynaptic readily releasable vesicle pool, and impaired synchronous auditory signalling as revealed by recordings of exocytic IHC capacitance changes and sound-evoked activation of spiral ganglion neurons. Both exocytosis of the hair cell releasable vesicle pool and the number of synchronously activated spiral ganglion neurons co-varied with the number of anchored ribbons during development. Interestingly, ribbon-deficient IHCs were still capable of sustained exocytosis with normal Ca^{2+} -dependence. Endocytic membrane retrieval was intact, but an accumulation of tubular and cisternal membrane profiles was observed in ribbon-deficient IHCs. We conclude that ribbon-dependent synchronous release of multiple vesicles at the hair cell afferent synapse is essential for normal hearing.

In addition, our study presents a molecularly defined mouse model for human auditory neuropathy and characterizes it as a synaptic audiopathy.

6. References

Altrock, W.D., tom Dieck, S., Sokolov, M., Meyer, A.C., Sigler, A., Brakebusch, C., Fassler, R., Richter, K., Boeckers, T.M., Potschka, H., Brandt, C., Loscher, W., Grimberg, D., Dresbach, T., Hempelmann, A., Hassan, H., Balschun, D., Frey, J.U., Brandstatter, J.H., Garner, C.C., Rosenmund, C., Gundelfinger, E.D. (2003). Functional inactivation of a fraction of excitatory synapses in mice deficient for the active zone protein bassoon. *Neuron* 37 (5), 787-800.

Ashmore, J.F. (1987). A fast motile response in guinea-pig outer hair cells: the cellular basis of the cochlear amplifier. *J Physiol* 388, 323-347.

Beutner, D. and Moser, T. (2001). The presynaptic function of mouse cochlea inner hair cells during development of hearing. *J Neurosci* 21 (13), 4593-4599.

Beutner, D., Voets, T., Neher, E. and Moser, T. (2001). Calcium dependence of exocytosis and endocytosis at the cochlear inner hair cell afferent synapse. *Neuron* 29, 681-690.

Breckenridge, L. J. and Almers, W. (1987). Final steps in exocytosis observed in a cell with giant secretory granules. *Proc Natl Acad Sci USA* 84, 1945-1949.

Brown, M.C. (1987). Morphology of labeled efferent fibers in the guinea pig cochlea. *J Comp Neurol* 260 (4), 605-618.

Chan, D.K. and Hudspeth, A.J. (2005). Ca(2+) current-driven nonlinear amplification by the mammalian cochlea in vitro. *Nat Neurosci* 8 (2), 149-155.

Corey, D.P., Garcia-Anoveros, J., Holt, J.R., Kwan, K.Y., Lin, S.Y., Vollrath, M.A., Amalfitano, A., Cheung, E.L., Derfler, B.H., Duggan, A., Geleoc, G.S., Gray, P.A., Hoffman, M.P., Rehm, H.L., Tamasauskas, D., Zhang, D.S. (2004). TRPA1 is a candidate for the mechanosensitive transduction channel of vertebrate hair cells. *Nature* 432 (7018), 723-730.

Dallos, P. and Fakler, B. (2002). Prestin, a new type of motor protein. *Nat Rev Mol Cell Biol* 3 (2), 104-111.

Dallos, P., Popper, A.N., Fay, R. (1996). *The Cochlea*. Springer, New York 44-258, 318-503.

Dick, O., Hack, I., Altrock, W.D., Garner, C.C., Gundelfinger, E.D., Brandstatter, J.H. (2001). Localization of the presynaptic cytomatrix protein Piccolo at ribbon and conventional synapses in the rat retina: comparison with Bassoon. *J Comp Neurol* 439 (2), 224-234.

References

- Dick, O., tom Dieck, S., Altrock, W.D., Ammermuller, J., Weiler, R., Garner, C.C., Gundelfinger, E.D., Brandstatter, J.H. (2003). The presynaptic active zone protein bassoon is essential for photoreceptor ribbon synapse formation in the retina. *Neuron* 37 (5), 775-786.
- Edmonds, B. W., Gregory, F. D. and Schweizer, F. E. (2004). Evidence that fast exocytosis can be predominantly mediated by vesicles not docked at active zones in frog saccular hair cells. *J Physiol* 560, 439-450.
- Egner, A., Jakobs, S. and Hell, S. W. (2002). Fast 100-nm resolution three-dimensional microscope reveals structural plasticity of mitochondria in live yeast. *Proc Natl Acad Sci USA* 99, 3370-3375.
- Emmerling, M.R., Sobkowicz, H.M., Levenick, C.V., Scott, G.L., Slapnick, S.M., Rose, J.E. (1990). Biochemical and morphological differentiation of acetylcholinesterase-positive efferent fibers in the mouse cochlea. *J Electron Microsc Tech* 15 (2), 123-143.
- Evans, B.N. and Dallos, P. (1993). Stereocilia displacement induced somatic motility of cochlear outer hair cells. *Proc Natl Acad Sci USA* 90 (18), 8347-8351.
- Eybalin, M. (1993). Neurotransmitters and neuromodulators of the mammalian cochlea. *Physiol Rev* 73 (2), 309-373.
- Eybalin, M., Caicedo, A., Renard, N., Ruel, J., Puel, J.L. (2004). Transient Ca²⁺-permeable AMPA receptors in postnatal rat primary auditory neurons. *Eur J Neurosci* 20 (11), 2981-2989.
- Eybalin, M., Renard, N., Aure, F., Safieddine, S. (2002). Cysteine-string protein in inner hair cells of the organ of Corti: synaptic expression and upregulation at the onset of hearing. *Eur J Neurosci* 15 (9), 1409-1420.
- Fenster, S.D., Chung, W.J., Zhai, R., Cases-Langhoff, C., Voss, B., Garner, A.M., Kaempfer, U., Kindler, S., Gundelfinger, E.D., Garner, C.C. (2000). Piccolo, a presynaptic zinc finger protein structurally related to bassoon. *Neuron* 25 (1), 203-214.
- Frank, G., Hemmert, W., Gummer, A.W. (1999). Limiting dynamics of high-frequency electromechanical transduction of outer hair cells. *Proc Natl Acad Sci USA* 96 (8), 4420-4425.
- Frankenhaeuser, B. and Hodgkin, A.L. (1957). The action of calcium on the electrical properties of squid axons. *J Physiol* 137, 218-244.
- Friedman, H.V., Bresler, T., Garner, C.C., Ziv, N.E. (2000). Assembly of New Individual Excitatory Synapses: Time Course and Temporal Order of Synaptic Molecule Recruitment. *Neuron* 27 (1), 57-69.

References

- Fuchs, P.A., Evans, M.G., Murrow, B.W. (1990). Calcium currents in hair cells isolated from the cochlea of the chick. *J Physiol* 429, 553-568.
- Fuchs, P.A., Glowatzki, E. and Moser, T. (2003). The afferent synapse of cochlear hair cells. *Curr Opin Neurobiol* 13, 452-458.
- Glowatzki, E., Fuchs, P.A. (2000). Cholinergic synaptic inhibition of inner hair cells in the neonatal mammalian cochlea. *Science* 288 (5475), 2366-2368.
- Glowatzki, E. and Fuchs, P.A. (2002). Transmitter release at the hair cell ribbon synapse. *Nat Neurosci* 5 (2), 147-154.
- Guinan, J.Jr., Warr, W.B., Norris, B.E. (1984). Topographic organization of the olivocochlear projections from the lateral and medial zones of the superior olivary complex. *J Comp Neurol* 226 (1), 21-27.
- Heidelberger, R., Sterling, P., and Matthews, G. (2002). Role of ATP in depletion and replenishment of the releasable pool of synaptic vesicles. *J Neurophysiol* 88, 98-106.
- Heidelberger, R., Heinemann, C., Neher, E. and Matthews, G. (1994). Calcium dependence of the rate of exocytosis in a synaptic terminal. *Nature* 371 (6497), 513-515.
- Hell, S. and Stelzer, E.H.K. (1992). Properties of a 4Pi-confocal fluorescence microscope. *J Opt Soc Am A Opt Image Sci Vis* 18, 2159-2166.
- Hibino, H., Pironkova, R., Onwumere, O., Vologodskaya, M., Hudspeth, A.J., Lesage, F. (2002). RIM binding proteins (RBPs) couple Rab3-interacting molecules (RIMs) to voltage-gated Ca(2+) channels. *Neuron* 34 (3), 411-423.
- Holt, M., Cooke, A., Wu, M. M. and Lagnado, L. (2003). Bulk membrane retrieval in the synaptic terminal of retinal bipolar cells. *J Neurosci* 23, 1329-1339.
- Horn, R., Marty, A. (1988). Muscarinic activation of ionic currents measured by a new whole-cell recording method. *J Gen Physiol* 92 (2), 145-159.
- Hudspeth, A. (1997). Mechanical amplification of stimuli by hair cells. *Curr Opin Neurobiol* 7 (4), 480-486.
- Hudspeth, A. (1997). How hearing happens. *Neuron* 19 (5), 947-950.
- Hudspeth, A.J., Corey, D.P. (1977). Sensitivity, polarity, and conductance change in the response of vertebrate hair cells to controlled mechanical stimuli. *Proc Natl Acad Sci USA* 74 (6), 2407-2411.

References

- Johnson, S.L., Marcotti, W., Kros, C.J. (2005). Increase in efficiency and reduction in Ca²⁺ dependence of exocytosis during development of mouse inner hair cells. *J Physiol* 15, 177-191.
- Kachar, B., Brownell, W.E., Altschuler, R., Fex, J. (1986). Electrokinetic shape changes of cochlear outer hair cells. *Nature* 322 (6077), 365-368.
- Kandel, E.R., Schwartz, J.H., Jessel, T.M. (2000). *Principles of Neural Science*. McGraw-Hill Companies, USA 590- 624.
- Kataoka, Y., Ohmori, H. (1994). Activation of glutamate receptors in response to membrane depolarization of hair cells isolated from chick cochlea. *J Physiol* 477 (3), 403-414.
- Kataoka, Y., Ohmori, H. (1996). Of known neurotransmitters, glutamate is the most likely to be released from chick cochlear hair cells. *J Neurophysiol* 76 (3), 1870-1879.
- Katz, P.S., Kirk, M.D., Govind, C.K. (1993). Facilitation and depression at different branches of the same motor axon: evidence for presynaptic differences in release. *J Neurosci* 13 (7), 3075-3089.
- Kemp, D.T. (1978). Stimulated acoustic emissions from within the human auditory system. *J Acoust Soc Am* 64, 1386-1391.
- Kennedy, H.J., Crawford, A.C., Fettiplace, R. (2005). Force generation by mammalian hair bundles supports a role in cochlear amplification. *Nature* 433 (7028), 880-883.
- Khimich, D., Nouvian, R., Pujol, R., tom Dieck, S., Egner, A., Gundelfinger E.D. and Moser, T. (2005). Hair Cell Synaptic Ribbons are Essential for Synchronous Auditory Signaling. *Nature* in press.
- Kros, C.J., Crawford, A.C. (1990). Potassium currents in inner hair cells isolated from the guinea-pig cochlea. *J Physiol* 421, 263-291.
- Kros, C.J., Ruppersberg, J.P., Rusch, A. (1998). Expression of a potassium current in inner hair cells during development of hearing in mice. *Nature* 394 (6690), 281-284.
- Kubisch, C., Schroeder, B.C., Friedrich, T., Lutjohann, B., El-Amraoui, A., Marlin, S., Petit, C., Jentsch, T.J. (1999). KCNQ4, a novel potassium channel expressed in sensory outer hair cells, is mutated in dominant deafness. *Cell* 96 (3), 437-446.
- Lagnado, L. (2003). Ribbon synapses. *Curr Biol* 13(16), R631.
- Langer, P., Grunder, S., Rusch, A. (2003). Expression of Ca²⁺-activated BK channel mRNA and its splice variants in the rat cochlea. *J Comp Neurol* 455 (2), 198-209.

References

- Lenzi, D., Crum, J., Ellisman, M.H. and Roberts, W.M. (2002). Depolarization redistributes synaptic membrane and creates a gradient of vesicles on the synaptic body at a ribbon synapse. *Neuron* 36 (4), 649-659.
- Lenzi, D., Runyeon, J.W., Crum, J., Ellisman, M.H., Roberts, W.M. (1999). Synaptic vesicle populations in saccular hair cells reconstructed by electron tomography. *J Neurosci* 19 (1), 119-132.
- Lenzi, D., von Gersdorff, H. (2001). Structure suggests function: the case for synaptic ribbons as exocytotic nanomachines. *Bioessays* 23 (9), 831-840.
- Liberman, M.C. (1982). Single-neuron labeling in the cat auditory nerve. *Science* 216, 1239-1241.
- Liberman, M.C., Dodds, L.W., Pierce, S. (1990). Afferent and efferent innervation of the cat cochlea: quantitative analysis with light and electron microscopy. *J Comp Neurol* 301 (3), 443-460.
- Liberman, M.C., Gao, J., He, D.Z., Wu, X., Jia, S., Zuo, J. (2002). Prestin is required for electromotility of the outer hair cell and for the cochlear amplifier. *Nature* 419 (6904), 300-304.
- Lindau, M., Neher, E. (1988). Patch-clamp techniques for time-resolved capacitance measurements in single cells. *Pflugers Arch* 411 (2), 137-146.
- Lohi, H., Kujala, M., Kerkela, E., Saarialho-Kere, U., Kestila, M., Kere, J. (2000). Mapping of five new putative anion transporter genes in human and characterization of SLC26A6, a candidate gene for pancreatic anion exchanger. *Genomics* 70 (1), 102-112.
- Lysakowski, A. (1996). Synaptic organization of the crista ampullaris in vertebrates. *Ann N Y Acad Sci* 781, 164-182.
- Marcotti, W., Johnson, S.L., Holley, M.C., Kros, C.J. (2003). Developmental changes in the expression of potassium currents of embryonic, neonatal and mature mouse inner hair cells. *J Physiol* 548 (2), 383-400.
- Marcotti, W., Johnson, S.L., Kros, C.J. (2004). Effects of intracellular stores and extracellular Ca(2+) on Ca(2+)-activated K(+) currents in mature mouse inner hair cells. *J Physiol* 557 (2), 613-633.
- Marcus, D.C., Wu, T., Wangemann, P., Kofuji, P. (2002). KCNJ10 (Kir4.1) potassium channel knockout abolishes endocochlear potential. *Am J Physiol Cell Physiol* 282 (2), 403-407.
- Martinez-Dunst, C., Michaels, R.L., Fuchs, P.A. (1997). Release sites and calcium channels in hair cells of the chick's cochlea. *J Neurosci* 17 (23), 9133-9144.

References

- Matsubara, A., Laake, J.H., Davanger, S., Usami, S., Ottersen, O.P. (1996). Organization of AMPA receptor subunits at a glutamate synapse: a quantitative immunogold analysis of hair cell synapses in the rat organ of Corti. *J Neurosci* 16 (14), 4457-4467.
- McNulty, J.A., Fox, L.M. (1992). Pinealocyte synaptic ribbons and neuroendocrine function. *Microsc Res Tech* 21 (3), 175-187.
- Merchan-Perez, A., Liberman, M.C. (1996). Ultrastructural differences among afferent synapses on cochlear hair cells: correlations with spontaneous discharge rate. *J Comp Neurol* 371 (2), 208-221.
- Moser, T. and Beutner, D. (2000). Kinetics of exocytosis and endocytosis at the cochlear inner hair cell afferent synapse of the mouse. *Proc Natl Acad Sci USA* 97 (2), 883-888.
- Muresan, V., Lyass, A., and Schapp, B.J., (1999). The kinesin motor Kif3A is a component of the presynaptic ribbon in vertebrate photoreceptors. *J. Neurosci* 19, 1027-1037.
- Neher, E. (1998). Vesicle pools and Ca²⁺ microdomains: new tools for understanding their roles in neurotransmitter release. *Neuron* 20 (3), 389-399.
- Neher, E., Marty, A. (1982). Discrete changes of cell membrane capacitance observed under conditions of enhanced secretion in bovine adrenal chromaffin cells. *Proc Natl Acad Sci USA* 79 (21), 6712-6716.
- Ohtsuka, T., Takao-Rikitsu, E., Inoue, E., Inoue, M., Takeuchi, M., Matsubara, K., Deguchi-Tawarada, M., Satoh, K., Morimoto, K., Nakanishi, H., Takai, Y. (2002). Cast: a novel protein of the cytomatrix at the active zone of synapses that forms a ternary complex with RIM1 and munc13-1. *J Cell Biol* 158 (3), 577-590.
- Oliver, D., He, D.Z., Klocker, N., Ludwig, J., Schulte, U., Waldegger, S., Ruppersberg, J.P., Dallos, P., Fakler, B. (2001). Intracellular anions as the voltage sensor of prestin, the outer hair cell motor protein. *Science* 292 (5525), 2340-2343.
- Oliver, D., Knipper, M., Derst, C., Fakler, B. (2003). Resting potential and submembrane calcium concentration of inner hair cells in the isolated mouse cochlea are set by KCNQ-type potassium channels. *J Neurosci* 23 (6), 2141-2149.
- Paillart, C., Li, J., Matthews, G. and Sterling, P. (2003). Endocytosis and vesicle recycling at a ribbon synapse. *J Neurosci* 23 (10), 4092-4099.
- Parsons, T.D., Sterling, P. (2003). Synaptic ribbon. Conveyor belt or safety belt? *Neuron* 37 (3), 379-382.

References

- Pickles, J.O., Comis, S.D., Osborne, M.P. (1984). Cross-links between stereocilia in the guinea pig organ of Corti, and their possible relation to sensory transduction. *Hear Res* 15 (2), 103-112.
- Platzer, J., Engel, J., Schrott-Fischer, A., Stephan, K., Bova, S., Chen, H., Zheng, H., Striessnig, J. (2000). Congenital deafness and sinoatrial node dysfunction in mice lacking class D L-type Ca²⁺ channels. *Cell* 102 (1), 89-97.
- Rao-Mirotznik, R., Harkins, A.B., Buchsbaum, G., Sterling, P. (1995). Mammalian rod terminal: architecture of a binary synapse. *Neuron* 14 (3), 561-569.
- Richter, K., Langnaese, K., Kreutz, M.R., Olias, G., Zhai, R., Scheich, H., Garner, C.C., Gundelfinger, E.D. (1999). Presynaptic cytomatrix protein bassoon is localized at both excitatory and inhibitory synapses of rat brain. *J Comp Neurol* 408 (3), 437-448.
- Roberts, W.M., Jacobs, R.A., Hudspeth, A.J. (1990). Colocalization of ion channels involved in frequency selectivity and synaptic transmission at presynaptic active zones of hair cells. *J Neurosci* 10 (11), 3664-3684.
- Raphael, Y., Altschuler, R.A. (2003). Structure and innervation of the cochlea. *Brain Res Bull* 60 (5-6), 397-422.
- Safieddine, S., Wenthold, R.J. (1999). SNARE complex at the ribbon synapses of cochlear hair cells: analysis of synaptic vesicle- and synaptic membrane-associated proteins. *Eur J Neurosci* 11 (3), 803-812.
- Shnerson, A., Devigne, C. and Pujol, R. (1981). Age-related changes in the C57BL/6J mouse cochlea. II. Ultrastructural findings. *Brain Res* 254, 77-88.
- Schmitz, F., Bechmann, M., and Drenckhahn, D. (1996). Purification of Synaptic Ribbons, Structural Components of the Photoreceptor Active Zone Complex. *J Neuroscience* 16 (22), 7109-7116.
- Schmitz, F., Konigstorfer, A. and Sudhof, T.C. (2000). RIBEYE, a component of synaptic ribbons: a protein's journey through evolution provides insight into synaptic ribbon function. *Neuron* 28 (3), 857-872.
- Siegel, J.H., Brownell, W.E. (1981). Presynaptic bodies in outer hair cells of the chinchilla organ of Corti. *Brain Res* 220 (1), 188-193.
- Siemens, J., Lillo, C., Dumont, R.A., Reynolds, A., Williams, D.S., Gillespie, P.G., Muller, U. (2004). Cadherin 23 is a component of the tip link in hair-cell stereocilia. *Nature* 428 (6986), 950-955.

References

- Simmons, D.D., Moulding, H.D., Zee, D. (1996). Olivocochlear innervation of inner and outer hair cells during postnatal maturation: an immunocytochemical study. *Brain Res Dev Brain Res* 95 (2), 213-226.
- Smith, J.E. and Reese, T.S. (1980). Use of aldehyde fixatives to determine the rate of synaptic transmitter release. *J Exp Biol* 89, 19-29.
- Smith, C.A. and Sjostrand, F. S. (1961). A synaptic structure in the hair cells of the guinea pig cochlea. *J Ultrastruct Res* 5, 184-192.
- Sobin, A. and Flock, A. (1983). Immunohistochemical identification and localization of actin and fimbrin in vestibular hair cells in the normal guinea pig and in a strain of the waltzing guinea pig. *Acta Otolaryngol* 96 (5-6), 407-412.
- Sobkowicz, H.M., Rose, J.E., Scott, G.L., Levenick, C.V. (1986). Distribution of synaptical ribbons in the developing organ of corti. *J. Neurocytol* 15 (6), 693-714.
- Sobkowicz, H.M., Slapnick, S.M. (1994). The efferents interconnecting auditory inner hair cells. *Hear Res* 75 (1-2), 81-92.
- Sollner, C., Rauch, G.J., Siemens, J., Geisler, R., Schuster, S.C., Muller, U., Nicolson, T. (2004). Mutations in cadherin 23 affect tip links in zebrafish sensory hair cells. *Nature* 428 (6986), 955-959.
- Spassova, M.A., Avissar, M., Furman, A.C., Crumling, M.A., Saunders, J.C., Parsons, T.D. (2004). Evidence That Rapid Vesicle Replenishment of the Synaptic Ribbon Mediates Recovery from Short-Term Adaptation at the Hair Cell Afferent Synapse. *J Assoc Res Otolaryngol* 5 (4), 376-390.
- Spiwox-Becker, I., Glas, M., Lasarzik, I., Vollrath, L. (2004). Mouse photoreceptor synaptic ribbons lose and regain material in response to illumination changes. *Eur J Neurosci* 19 (6), 1559-1571.
- Starr, A., Picton, T.W., Sininger, Y., Hood, L.J. and Berlin, C.I. (1996). Auditory neuropathy. *Brain* 119 (3), 741-753.
- Sterling, P. and Matthews, G. (2005). Structure and function of ribbon synapses. *Trends Neurosci* 28 (1), 20-29.
- Takao-Rikitsu, E., Mochida, S., Inoue, E., Deguchi-Tawarada, M., Inoue, M., Ohtsuka, T., Takai, Y. (2004). Physical and functional interaction of the active zone proteins, CAST, RIM1, and Bassoon, in neurotransmitter release. *J Cell Biol* 164 (2), 301-311.
- tom Dieck, S., Altroch, W.D., Kessels, M.M., Qualmann, B., Regus, H., Brauner, D., Fejtova, A., Bracko, O., Gundelfinger, E.D., Brandstatter, J.H. (2005). Molecular dissection

References

of the photoreceptor ribbon synapse: physical interaction of Bassoon and RIBEYE is essential for the assembly of the ribbon complex. *J Cell Biol* 168 (5), 825-836.

tom Dieck, S., Sanmarti-Vila, L., Langnaese, K., Richter, K., Kindler, S., Soyke, A., Wex, H., Smalla, K.H., Kampf, U., Franzer, J.T., Stumm, M., Garner, C.C., Gundelfinger, E.D. (1998). Bassoon, a novel zinc-finger CAG/glutamine-repeat protein selectively localized at the active zone of presynaptic nerve terminals. *J Cell Biol* 142 (2), 499-509.

Trussell, L. O. (1999). Synaptic mechanisms for coding timing in auditory neurons [In Process Citation]. *Annu Rev Physiol* 61, 477-496.

Turner, J., and M. Crossley. (2001). The CtBP family: enigmatic and enzymatic transcriptional co-repressors. *Bioessays* 8, 683-690.

Kros, C.J. (1996) in *The Cochlea*, eds. Dallos, P., Popper, A.N.&Fay, R.R. (Springer, New York), pp.318-385

Usukura, J., Yamada, E. (1987). Ultrastructure of the synaptic ribbons in photoreceptor cells of *Rana catesbeiana* revealed by freeze-etching and freeze-substitution. *Cell Tissue Res* 247 (3), 483-488.

Voets, T., Neher, E., Moser, T., (1999). Mechanisms underlying phasic and sustained secretion in chromaffin cells from mouse adrenal slices. *Neuron* 23 (3), 607-615.

Vollrath, L., Spiwox-Becker, I. (1996). Plasticity of retinal ribbon synapses. *Microsc Res Tech* 35 (6), 472-487.

von Gersdorff, H. (2001). Synaptic ribbons: versatile signal transducers. *Neuron* 29 (1), 7-10.

von Gersdorff, H., Matthews, G. (1999). Electrophysiology of synaptic vesicle cycling. *Annu Rev Physiol* 61, 725-752.

von Gersdorff, H., Vardi, E., Matthews, G. and Sterling, P. (1996). Evidence that vesicles on the synaptic ribbon of retinal bipolar neurons can be rapidly released. *Neuron* 16 (6), 1221-1227.

Wagner, H.J., (1997). Presynaptic bodies ("ribbons"): from ultrastructural observations to molecular perspectives. *Cell Tissue Res* 287 (3), 435-446.

Wang, X., Kibschul, I. M., Laue, M.M., Lichte, B., Petrasch-Parwez, E., Kilimann, M.W. (1999) Aczonin, a 550-kD putative scaffolding protein of presynaptic active zones, shares homology regions with Rim and Bassoon and binds profilin. *J Cell Biol* 147 (1), 151-162.

Wang, Y., Okamoto, M., Schmitz, F., Hofmann, K., Sudhof, T.C. (1997). Rim is a putative Rab3 effector in regulating synaptic-vesicle fusion. *Nature* 388 (6642), 593-598.

References

- Weigert, R., M.G. Silletta, S. Spanò, G. Turacchio, C. Cericola, A. Colanzi, S. Senatore, R. Mancini, E.V. Polishchuk, M. Salmons, et al. (1999). CtBP/BARS induces fission of Golgi membranes by acylating lysophosphatidic acid. *Nature* 402 (6760), 429-433.
- White, J.S., Warr, W.B. (1983). The dual origins of the olivocochlear bundle in the albino rat. *J Comp Neurol* 219 (2), 203-214.
- Zenisek, D., Horst, N.K., Merrifield, C., Sterling, P., Matthews, G. (2004). Visualizing synaptic ribbons in the living cell. *J Neurosci* 24 (44), 9752-9759.
- Zenisek, D., Steyer, J. A. and Almers, W. (2000). Transport, capture and exocytosis of single synaptic vesicles at active zones. *Nature* 406 (6798), 849-854.
- Zhai, R.G., Vardinon-Friedman, H., Cases-Langhoff, C., Becker, B., Gundelfinger, E.D., Ziv, N.E., and Garner, C.C. (2001). Assembling the presynaptic active zone: a characterization of an active zone precursor vesicle. *Neuron* 29 (1), 131-143
- Zheng, J., Shen, W., He, D.Z., Long, K.B., Madison, L.D., Dallos, P. (2000). Prestin is the motor protein of cochlear outer hair cells. *Nature* 405 (6783), 149-155.
- Zheng, J., Madison, L.D., Oliver, D., Fakler, B., Dallos, P. (2002). Prestin, the motor protein of outer hair cells. *Audiol Neurootol* 7 (1), 9-12.

Acknowledgements

I would like to thank Prof. Tobias Moser for the given possibility to work on this project, for his generous help and constant support.

I am very grateful to the members of my thesis committee Prof. Erwin Neher and Prof. Norbert Elsner for their interest, critical feedback and many useful advices.

Many warm thanks to my colleagues from the InnerEarLab for the very friendly working environment, discussions, help and fun. Special thanks to Andreas Brandt and Primoz Pirih for providing custom analysis software and Dr. Regis Nouvian for common work on Bassoon project. Thanks to Margitta Köppler for the expert technical assistance and Dr. Arglebe for reading my thesis.

I am grateful to our collaborators: Prof. Remy Pujol from Montpellier (for electron microscopy), Dr. Alexander Egnér and Dr. Andreas Schönle from the MPI for Biophysical Chemistry (4Pi microscopy), and Dr. Frank Kirchhoff for the possibility to work on their confocal microscope.

Thanks to the Neuroscience office coordinators for their persistent organizational help and colleagues from the Neuroscience program for discussion of the progress reports, warm meetings and friendly support.

This work was supported by a SFB 406 grant to Prof. Tobias Moser.

Curriculum vitae

Name	Darina Khimich
Date of birth	23 December 1976
Citizenship	Ukrainian
Education	1984 - 1992 Middle school 1992 - 1994 Student at the Medical Lyceum, Kiev 1994 - 2000 Student at the National Medical University, Dept. of General Medicine, Kiev 2000 - 2001 MSc study year at the International Neuroscience program, Göttingen 2001 - 2005 MD-PhD project in the framework of the International Neuroscience Program, InnerEarLab at the Dept. of Otolaryngology and Center for Molecular Physiology of the Brain, Göttingen

Publications

Khimich, D., Nouvian, R., Pujol, R., tom Dieck, S., Egner, A., Gundelfinger E.D. and Moser, T. (2005). Hair Cell Synaptic Ribbons are Essential for Synchronous Auditory Signaling. *Nature* in press.

Schmitz, F., Tabares, L., Khimich, D., de la Villa-Polo, P., Strenzke, N., Castellano-Muñoz, M., Moser, T., Fernández-Chacón, R. and Südhof, T.C. Retinal Degeneration in CSP α -deficient mice, to be submitted.

Curriculum vitae

Kharkovets, T., Dedek, K., Schweizer, M., Maier, H., Khimich, D., Nouvian, R., Moser, T., Leuwer, R. and Jentsch, T.J. Mice with modified KCNQ4 K⁺ channels as models for DFNA2 deafness, to be submitted.

Khimich, D., Pirih, P., Wolf, F. and Moser, T. Quantal Analysis of Synaptic Vesicle Exocytosis at the Hair Cell Ribbon Synapse, in prep.